Monthly Mean Sea-Level Variability Along the West Coast of North America

DUDLEY B. CHELTON

Jet Propulsion Laboratory, California Institute of Technology, Pasadena 91109

RUSS E. DAVIS

Scripps Institution of Oceanography, La Jolla, CA 92093

(Manuscript received 29 October 1980, in final form 3 May 1982)

ABSTRACT

Linear statistical estimators are used to examine 29 years of nonseasonal, monthly-mean, tide-gauge sea-level data along the west coast of North America. The objective is exploration of the structure and causes of nearshore ocean variability over time scales of months to years at 20 stations from Alaska to Mexico. North of San Francisco, 50–60% of the sea-level variability reflects a simple inverse barometric response to local atmospheric pressure. These inverted barometer effects account for only 10–15% of the variance at stations to the south.

The dominant signal of inverse-barometer-corrected sea level represents a nearly uniform rise or fall of sea level everywhere along the eastern rim of the North Pacific. The interannual aspects of this large-scale sea-level variability are closely related to El Niño occurrences in the eastern tropical Pacific which appear to propagate poleward with phase speeds of $\sim$40 cm s^{-1}. Higher frequency aspects of this large-scale sea-level variability appear to represent quasi-geostrophic currents driven by basin-wide scales of wind forcing over the North Pacific.

The nature of local (individual station) inverse-barometer-corrected sea-level variability is examined through a series of statistical models and the results are compared with existing dynamical models. The longshore component of wind stress generally forces a larger response than the onshore component (except in large semi-enclosed basins) but the important dynamical aspects of the wind field appear to be basin wide rather than local. The response is consistent with that expected from Ekman dynamics. An apparent non-barometric response to local atmospheric pressure is shown to partly represent an influence of sea-level anomalies farther south. Efforts to determine the nature of this indirect coupling between local pressure and sea level at stations to the south are somewhat limited by the ability of statistical estimators to accurately isolate the responses of sea level to a number of correlated inputs. However, evidence is presented indicating that part of the apparent non-barometric response is due to longshore wind-stress forcing at stations to the south. A response 30–50% greater than inverse barometric remains unexplained from Tofino to San Francisco.

1. Introduction

Description of the causes of low-frequency coastal oceanic variability is hindered by an absence of suitable observations of coastal currents. On relatively short time scales velocity observations permit direct examination of coastal dynamics, but current-meter records of sufficient length to examine variability with time scales of months to years do not exist. While not as directly descriptive of dynamics as velocity, sea surface elevation can be used to describe low-frequency coastal variability because tide-gauge measurements have been routinely recorded at numerous locations over extended periods of time.

A number of theoretical and observational studies over the last few years have focused on variability of sea-level height (SLH) over time scales of days to weeks. The results, reviewed by Clarke (1977), indicate the importance of propagating coastal trapped waves, both forced and free. Less is known about SLH variability over longer time scales. In this study, monthly anomalies (deviations from the mean seasonal cycle) of tide-gauge measured SLH are used to examine coastal dynamics over short-term climatic time scales of months to years.

Among the many causes of SLH variability, the most obvious is the local atmospheric pressure. Robinson (1964) showed from scaling arguments that the open ocean should respond as an inverse barometer to changes in atmospheric pressure, i.e., the sea surface is depressed 1 cm for each millibar of increased atmospheric pressure so that the net bottom pressure remains constant (isostatic). This has been verified by Brown *et al.* (1975) who found low coherence between bottom pressure and atmospheric pressure in the MODE experiment. Although it is somewhat difficult to tell from his logarithmic plots, Wunsch (1972) also appears to have demon-

0022-3670/82/080757-28$11.00

strated isostatic response at periods from about 2 days to 2 weeks from an analysis of eight years of SLH data at Bermuda. However, over a sloping bottom continental shelf region, the atmospheric pressure can force resonant continental shelf waves and the SLH response can differ significantly from inverse barometric (Robinson, 1964). Hamon (1966) and, more recently, Wang and Mooers (1977) have used these results to explain observed non-isostatic response of SLH along the coasts of Australia and Oregon, respectively.

Adams and Buchwald (1969) and Gill and Schumann (1974) have argued that the wind stress is one to two orders of magnitude more important than pressure in forcing low-frequency coastally trapped waves. They further argue that longshore wind stress is the principal driving mechanism and that the onshore component is relatively unimportant. The Ekman transport associated with coastal longshore winds results in convergence or divergence of water at the coast. Along eastern boundaries, these SLH anomalies then propagate poleward as the coastally trapped waves "adjust" the coastal region to the newly applied forcing.

It is apparent then that, in addition to a purely local response to wind stress, part of the SLH variability at any given location may be a non-locally generated response resulting from poleward propagation of freely travelling coastal trapped waves. Along the west coast of North America these waves may have been generated by coastal winds at locations farther south or, as suggested analytically by McCreary (1976) and numerically by Godfrey (1975) and Hurlburt *et al.* (1976), they may have originated in the tropics. Their results indicate that a weakening of the equatorial zonal wind field causes a rise in SLH in the eastern tropical Pacific which then spreads to higher latitudes along the eastern boundary as coastally trapped Kelvin waves. This models aspects of the anomalous condition known as El Niño which is observed to be a low-frequency phenomenon with "events" typically lasting a year or longer. Note that at the very low (interannual) frequencies associated with El Niño, there is an offshore "leakage" of the coastally trapped wave energy in the form of westward-propagating Rossby waves (Godfrey, 1975; McCreary, 1977; Cane and Sarachik, 1977). The signatures in west coast SLH of the stronger El Niño occurrences such as 1957–58 and 1972–73 have been noted from visual correlations by Bretschneider and McLain (1976). Enfield and Allen (1980) have more quantitatively demonstrated the presence of these El Niño related effects in west coast SLH through cross-spectral analysis with the Southern Oscillation Index.

Most earlier studies of monthly SLH variability have focused primarily on the seasonal cycle (long term mean of SLH for each month of the year). Strong resemblances to the seasonal cycles of other variables, primarily sea-level pressure (SLP) and nearshore steric height, have been noted. A global summary of the results has been presented by Pattullo *et al.* (1955). Dynamical interpretation of these observations is difficult because the seasonal cycles of all potential driving mechanisms are apt to be highly coherent with the seasonal cycle of SLH. The presence of these seasonal cycles reduces the number of independent observations in the sample records. It is therefore essential to remove the seasonal cycles of both sea-level and atmospheric data before attempting statistical examination of dynamical models.

Monthly anomalies of SLH (deviations from the seasonal cycle) along the west coast of the United States were first studied by Roden (1960, 1966). The essential results of his analyses are that: 1) there is large areal coherence of SLH (of the order 1200 km); 2) differences in exposure of the tide gauge, i.e., along the open coast or in enclosed bays, are relatively unimportant in terms of measuring monthly variations of SLH; 3) there is a moderate to poor coherence between SLH and local sea surface temperature; and 4) there is a strong inverse relationship between SLH and SLP with a response 1–2 times greater than the theoretical inverse barometric value. Saur (1962) also noted a larger than inverse barometric response and found that negative anomalies of SLP along the west coast are associated with stronger southerly winds. He suggested the additional response of SLH to negative SLP anomalies may be due to a piling-up of water along the coast caused by Ekman mass transport induced by the winds which are correlated with SLP.

The purpose of this analysis is to identify the important physical causes of SLH variability over monthly time scales and to compare the results with present notions about coastal dynamics. The statistical methods used are summarized in Section 2 and described more completely in Chelton (1982). They are designed to extract the true "signal" of covariation between one or more input fields and an output field (in this case SLH) from the noise of chance cooccurrence. Specifically, the analysis is aimed at answering the following questions: 1) Can west coast SLH be quantitatively related to eastern tropical Pacific El Niño occurrences? 2) Is there evidence for propagation of SLH anomalies along the coastline at these low frequencies? 3) Are local winds, particularly longshore winds, important for forcing low-frequency SLH changes? 4) Are basin-wide scales of atmospheric forcing important causes of SLH variability?

Determining the relative importance of local winds, large-scale winds and local atmospheric pressure is complicated by the fact that all are correlated. This is a result of the fact that the major atmospheric

variability can be described by a few dominant spatial patterns in each of which pressure and wind have a prescribed relation (see Davis, 1976). To avoid drawing erroneous conclusions about cause and effect, it is therefore essential that all potential atmospheric forcing parameters be included together in a multiple input statistical model rather than a series of single input models (simple correlations).

It has become customary in nearly all SLH investigations to correct SLH for the theoretical inverse barometric effect of SLP and look at the response of the residuals to wind stress. A recent example is the work of Enfield and Allen (1980). This *a priori* correction of SLH is justifiable on the grounds that the subsurface pressure (which can be directly related to the dynamics of the upper ocean) is the variable that is really of interest. However, conclusions about dynamics drawn from a statistical analysis might be misleading if it is assumed that the *only* response of SLH to SLP is isostatic. For example, if wind stress and SLP are correlated, part of an apparent response of inverse-barometer-corrected SLH to wind stress may really be due to non-isostatic effects of SLP which have not been included in the statistical model. The correct approach is to include SLP as an input variable in the statistical model for inverse-barometer-corrected SLH, thereby determining whether the response is, in fact, purely isostatic (in which case the response coefficient of SLP will be identically zero). So in addressing question 3 above in this study, the local pressure will be included as one of the parameters in a multiple-input statistical model for inverse-barometer-corrected SLH.

2. Dynamical versus statistical models

The statistical technique employed here to examine the physical causes of SLH variability is an application of minimum mean square error estimation. The motivation for using statistical estimators is not to develop a model for forecasting SLH but to investigate existing dynamical models of coastal SLH variability. The method is described in detail in Chelton (1982) and only a brief discussion will be given here. For present purposes the important feature of such models is that, if the system dynamics are linear and forced only by the inputs admitted in the statistical estimator, then the statistical model recovers the dynamical transfer functions between the inputs and output (Davis, 1977). In this study, all atmospheric parameters that potentially influence SLH are inter-correlated so it is not possible to look at the effect on SLH on each forcing individually, irrespective of the other forcings. Since an apparent correlation between SLH and another variable may result from each being separately correlated with a third variable, it is essential that the effects of all forcing functions be accounted for through a multiple-input statistical model rather than a series of single-input models.

SLH (the estimand) will be denoted by $h(t)$ and is assumed to be linearly related to M input variables $\tilde{d}_1, \ldots, \tilde{d}_M$. The theoretical frameworks discussed in the Introduction and in Section 6 provide guidance in the *a priori* selection of input variables. The objective is to make an estimate of the form

$$\hat{h}(t) = \sum_{m=1}^{M} \beta_m \tilde{d}_m(t + \tau_m).$$

A value of $\tau_m = 0$ represents a specification of sea level from forcing data during the same month while negative values of τ represent a prediction of sea level from prior forcing data. For ease of notation, we transform variables so that $d_m(t) = \tilde{d}_m(t + \tau_m)$. The response coefficients $\hat{\beta}_m$ that minimize the expected square error of the estimate are estimated over the finite record length by

$$\hat{\beta}_m = \sum_{n=1}^{M} \{d_m d_n\}^{-1}\{h d_n\},$$

where the braces denote the sample mean value and $\{d_m d_n\}^{-1}$ is the m, nth element of the inverse of the $M \times M$ mean product matrix of the inputs. It is shown in Chelton (1982) that the value of the response coefficient $\hat{\beta}_m$ obtained is that which would relate h and d_m if all other inputs except d_m were zero. Thus a multiple-input model is effectively a selective filter, extracting only the effect on the estimand of each input variable that results from a true relation between the two rather than from correlations of each with another input variable. If the dynamics of the system are linear, the response coefficients obtained in the multiple-input statistical model are those in the dynamical model.

The skill in hindcasting SLH over the data set from which the statistics are estimated is measured by the fraction of sample variance accounted for by the model, i.e.,

$$S_H = 1 - \frac{\{(h - \hat{h})^2\}}{\{h^2\}}$$

$$= \{h^2\}^{-1} \sum\sum \{d_m h\}\{d_m d_n\}^{-1}\{d_n h\}.$$

This sample hindcast estimate of the true estimation skill is inflated by sampling errors whose magnitude depends on the correlation time scales of the variables $h(t)$ and $d_m(t)$. Low-frequency components of these variables are not well sampled by short records and lead to sampling errors which, on average, make $h(t)$ appear more predictable than it is. In this study, forecasts over extremely long lags are used to estimate the mean artificial predictability $\langle S_A \rangle$ which is the mean S_H obtained when the true skill is be-

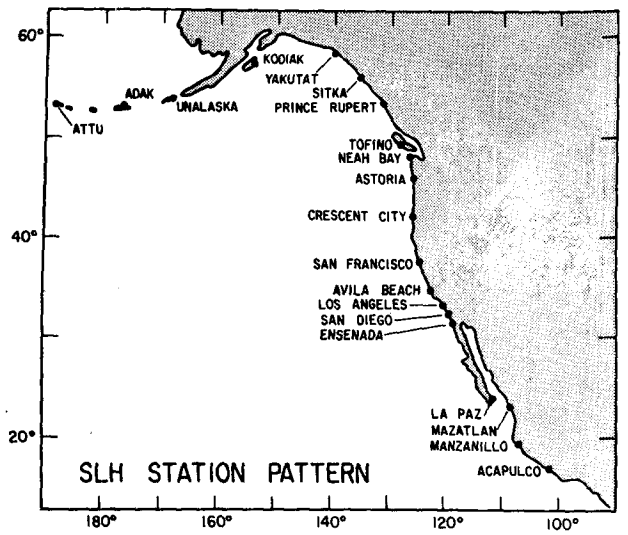

FIG. 1. Location of the 20 sea-level height (SLH) tide-gauge stations analyzed in this study.

lieved to vanish. If the true skill vanishes, the probability density of $MS_H/\langle S_A\rangle$ is approximately a chi-square distribution with M degrees of freedom; this can be used to establish significance levels of sample hindcast skill values.

The use of imperfect sample statistics also introduces uncertainty in the sample estimates of the response coefficients which increases with the number of inputs included in the model. The approximate $100(1-\alpha)$ percent confidence region for the true value β_m based on the sample estimate $\hat{\beta}_m$ is given by

$$(\beta_m - \hat{\beta}_m)^2 \leq \frac{1}{M}\frac{\langle S_A\rangle}{(1-S_m)}\frac{\{h^2\}}{\{d_m{}^2\}}R_M(\alpha)$$

$$= \frac{1}{N^*}\frac{(1-S_H)}{(1-S_m)}\frac{\{h^2\}}{\{d_m{}^2\}}R_M(\alpha),$$

where S_m represents the hindcast skill in estimating $d_m(t)$ from the other $M-1$ inputs, defined similar to S_H, N^* is the effective number of degrees of freedom in the data records, and $R_M(\alpha)$ is the 100α percentage point of a chi-square distribution with M degrees of freedom. The important point to be noted from this expression is that the accuracy of the estimated response coefficient $\hat{\beta}_m$ is degraded when $d_m(t)$ is highly correlated with the other inputs (i.e., when S_m is large). These results are intuitively appealing; when two inputs are highly correlated, it is difficult to separate the response of the estimand to each. It will be seen in Section 6 that this fact limits our ability to statistically determine the nature of atmospheric forcing responsible for part of the SLH response at any particular station; all of the potential aspects of atmospheric forcing are highly correlated.

3. Scale description

The region chosen for investigation of the questions outlined in the Introduction is the west coast of North America from the tip of the Aleutian Islands to southern Mexico. Tide-gauge sea-level records were provided by K. Wyrtki at the University of Hawaii. Monthly mean values of SLH from 1946 to 1974 for the 20 stations shown in Fig. 1 were chosen using length of time series and spatial distribution along the coastline as selection criteria. The number of months of sea-level data available at each station are given in Table 1. Complete records of SLH are desirable from the standpoint of data analysis. An attempt was made to objectively estimate data gaps from nearby "satellite" stations by a linear estimator of the form described in Section 2 but the expected square errors of the estimates were generally too large to be of any value (typically 25–50% of the variance). Rather than introduce any artificial correlations, the analysis techniques were designed to handle the gappy time series.

Monthly mean values of atmospheric data (sea-level pressure and surface wind stress) over the same 29-year time span were taken from Fleet Numerical Oceanography Center (FNOC) grids provided by A. Bakun at the National Marine Fisheries Service in Monterey, California. The basic FNOC data consists of 6 h values of SLP on a 63 × 63 Northern Hemisphere polar stereographic grid. Monthly mean values of SLP were computed by FNOC by averaging all the 6 h observations within each calendar month. The wind stress monthly means were derived by first computing the quasi-geostrophic wind stress from SLP at 6 h intervals and then averaging these 6 h wind-stress values to obtain monthly means (see Caton *et al.*, 1978). The wind-stress values used here were derived using a constant drag coefficient of 1.3×10^{-3}.

It is worth pointing out that the wind-stress data used in this study differ from those used by Enfield and Allen (1980). The Enfield and Allen monthly average wind stresses were computed directly from monthly average quasi-geostrophic wind vectors [see Bakun (1973) for details]. Because the stress calculation is nonlinear, the magnitude of the computed wind stress can be strongly dependent on the vector averaging period. For example, Fissel *et al.*, (1977) have shown that, for wind measurements at Ocean Weather Station P (50°N, 145°W), the magnitude of monthly average wind stress computed from monthly average wind vectors is less than one-half the value computed from 6 h average wind vectors. So, although it has not yet been demonstrated, the wind-stress data used in this study should be a better representation of the actual monthly mean wind stress than that used by Enfield and Allen (1980).

The first analysis step was to compute monthly

TABLE 1. Statistical characteristics of SLH at each of the 20 individual stations: N is the total number of months of data between 1946 and 1974; σ_1 the standard deviation of raw SLH, and σ_2 the standard deviation of SLH corrected for inverted barometer effects of atmospheric pressure. Trend refers to the least squares fit to a linear trend over the 29 years. The values of the four principal empirical orthogonal functions (EOFs) of SLH over these 20 stations are also given. Numbers in parentheses in column headings refer to percentage of overall variance explained by the corresponding EOF. Numbers in parentheses in columns refer to percentage of σ_2^2 explained at each individual station by the corresponding EOF.

Station	N	σ_1 (cm)	σ_2 (cm)	σ_2^2/σ_1^2	Trend (cm year^{-1})	EOF value (percent σ_2^2 explained) No. 1 (38)	No. 2 (18)	No. 3 (10)	No. 4 (9)
Attu	310	7.8	6.9	0.78	0.37	0.28 (2)	1.91 (35)	1.94 (19)	2.43 (12)
Adak	322	7.8	5.6	0.52	0.16	0.83 (22)	0.44 (3)	−2.02 (32)	1.99 (29)
Unalaska	317	9.3	6.1	0.43	−0.28	0.63 (11)	−1.77 (39)	−2.09 (29)	0.93 (5)
Kodiak	172	7.2	3.5	0.24	0.02	0.73 (44)	−0.53 (11)	−0.31 (2)	0.54 (6)
Yakutat	322	8.3	5.4	0.42	−0.29	0.59 (12)	−1.65 (43)	0.14 (0)	−0.57 (3)
Sitka	343	6.6	4.0	0.37	−0.10	0.71 (31)	−1.06 (33)	0.05 (0)	0.21 (3)
Prince Rupert	348	7.4	5.1	0.47	0.16	1.09 (44)	−0.32 (2)	0.14 (0)	1.01 (9)
Tofino	344	7.2	4.8	0.44	−0.02	1.14 (55)	−0.89 (16)	0.95 (9)	0.65 (4)
Neah Bay	336	7.5	5.2	0.48	−0.10	1.07 (42)	−1.25 (27)	1.09 (11)	0.60 (3)
Astoria	339	9.2 (6.8)*	5.7	0.70	−0.11	0.88 (24)	−1.31 (24)	1.54 (18)	0.17 (0)
Crescent City	324	6.4	4.7	0.54	−0.07	0.91 (37)	−0.70 (10)	0.69 (5)	0.22 (1)
San Francisco	348	5.5	4.5	0.67	0.22	0.92 (42)	0.79 (14)	0.05 (0)	0.74 (6)
Avila Beach	258	4.5	4.1	0.83	0.12	0.71 (30)	0.71 (14)	−1.09 (17)	0.57 (5)
Los Angeles	348	3.7	3.4	0.84	0.03	0.78 (52)	0.32 (4)	−0.58 (7)	−0.21 (1)
San Diego	339	4.1	3.8	0.86	0.15	0.92 (57)	0.78 (19)	−0.69 (8)	−0.01 (0)
Ensenada	205	3.6	3.3	0.84	0.03	0.77 (53)	0.30 (4)	−0.09 (0)	−0.19 (1)
La Paz	260	4.2	4.0	0.91	0.11	0.94 (53)	0.59 (10)	0.37 (2)	−0.03 (0)
Mazatlan	259	6.4	6.2	0.94	0.08	1.63 (69)	0.64 (5)	0.37 (2)	−1.40 (12)
Manzanillo	241	6.5	6.2	0.91	0.07	1.64 (70)	0.69 (6)	0.06 (0)	−1.59 (15)
Acapulco	309	6.7	6.5	0.94	0.11	1.61 (60)	1.03 (11)	−0.63 (2)	−1.12 (7)

* Corrected for effects of Columbia River outflow (see text).

anomalies of each variable. An anomaly for a given month is defined to be the departure of the observation from the long-term mean for that particular month. The mean annual cycle of SLH has been described by Enfield and Allen (1980) and the seasonal cycle of SLP has been described by O'Conner (1961). The discussion that follows deals only with anomalous aspects of the data.

The time series of sea-level anomalies are shown in Fig. 2. There are significant events that are coherent over extremely large distances. Most notable is the large positive anomaly of 1957–58 present at all stations south of Adak, Alaska. Distinct trends are also evident in some of the records, particularly at Unalaska, Yakutat, San Francisco and San Diego. These trends will be discussed further in Section 5. In addition, there are instances of apparent sudden datum level changes in the records at Attu, Adak and Unalaska followed by a gradual return to normal over a period of several years. Wahr and Wyss (1980) have related these datum level shifts to the occurrences of the great Aleutian earthquakes of 1957 and 1965. The time series have not been corrected for these datum level changes in the analysis that follows and so they enter the statistical models as noise.

The standard deviations of raw SLH are given in Table 1 and shown as the dashed line in Fig. 3. The variability is largest at Unalaska and generally decreases to the south and farther west in the Aleutian Islands. Typical values of SLH anomalies range from about 8 cm at the high-latitude stations to about 4 cm off southern California and about 6 cm along the mainland coast of Mexico. The notable departure from this general description is the exceptionally large standard deviation (about 20% higher than at neighboring stations) at Astoria, Oregon, located at the mouth of the Columbia River.

It has been suggested (Roden, 1960; Bretschneider and McLain, 1976) that fluctuations in Astoria SLH are not indicative of oceanic conditions but are instead a measure of the strength of river outflow. The Columbia River is the largest river along the Pacific coast of North America and consists of two major contributions: the Willamette River and the Upper Columbia River itself. Records of Willamette and Upper Columbia streamflow at Salem and The Dalles, respectively, were obtained from the USGS. These locations were chosen because they are the ones located nearest the confluence of the two rivers at Portland that cover the 29 years of SLH data examined here. Since there are no dams and no major tributaries downstream of Portland, the total outflow at Astoria was taken to be the sum of the flows of the Willamette and Upper Columbia Rivers. A multiple input statistical model was formulated, as discussed in Section 2, relating SLH at Astoria to Columbia River runoff and the large-scale and local-

atmospheric forcing parameters to be described in Section 6. It was assumed that Columbia River runoff is a true physical cause of SLH variability at Astoria and that the relationship between the two is not the result of each being related to some other forcing function not included in the model. When Astoria SLH is "corrected" for river runoff by removing the response to streamflow as determined from the multiple-input model, the standard deviation is reduced to a value comparable to that at neighboring stations to the north or south (see open circle in Fig. 3). Columbia River runoff accounts for 45% of the SLH variance at Astoria. This suggests that if Columbia River outflow is properly accounted

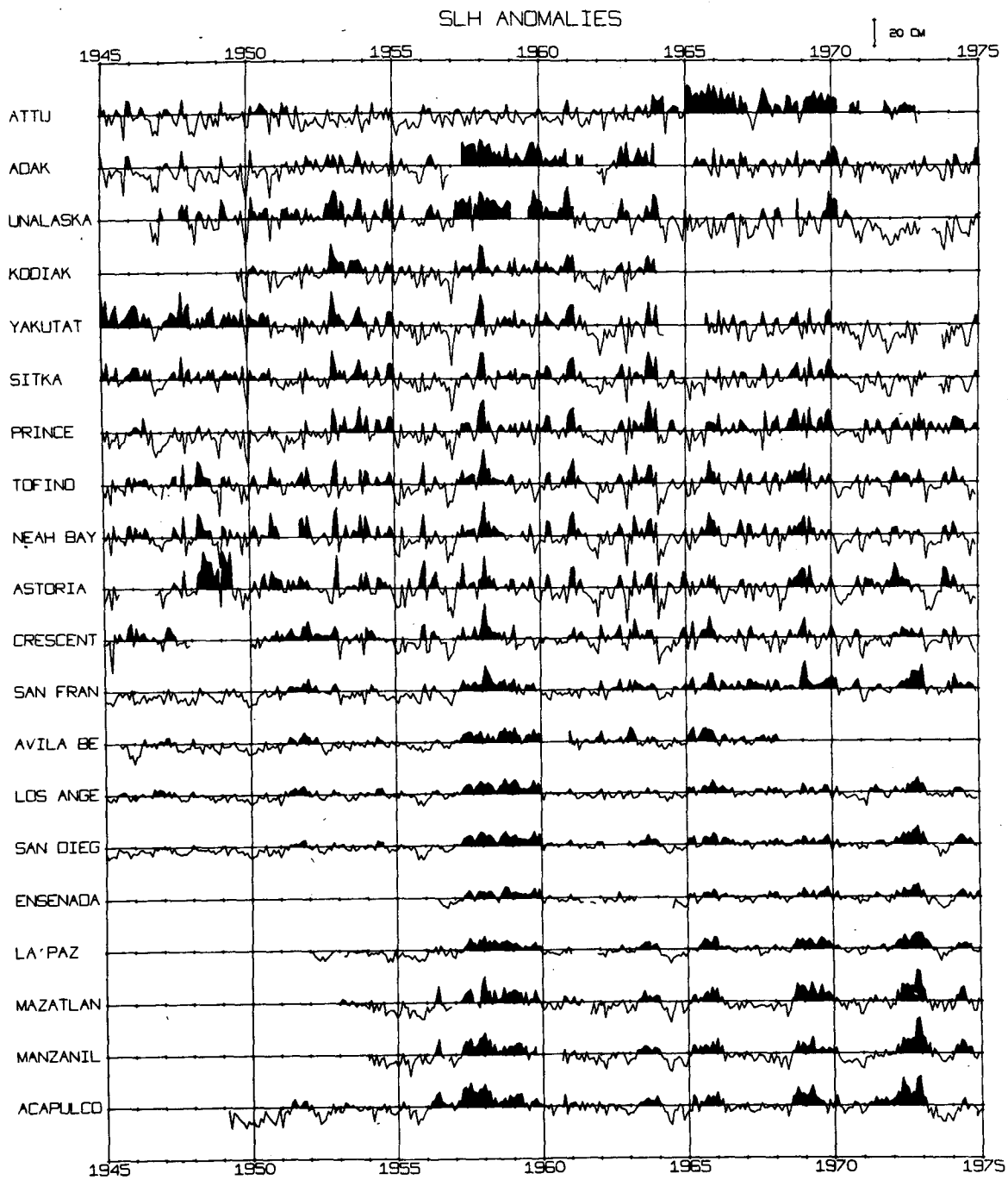

FIG. 2. Time series of SLH anomalies at each of the 20 tide-gauge stations. Tic marks are January and year labels are centered at January of that year. Dark areas correspond to positive anomalies and scale of vertical axis is shown in upper right hand corner of plot. Records have not been corrected for inverse barometric effects of atmospheric pressure.

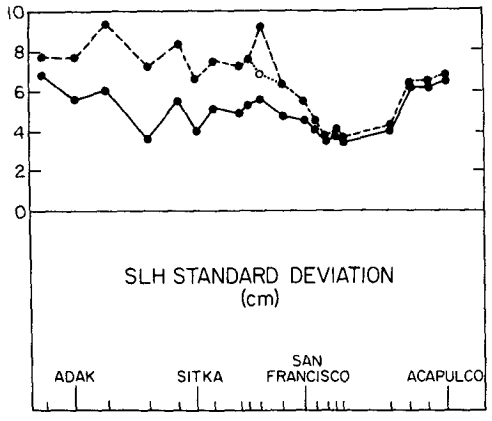

FIG. 3. Standard deviation of SLH. Tic marks indicate tide-gauge station locations. Dashed line is the standard deviation of raw SLH anomalies (open circle is the standard deviation at Astoria after effects of Columbia River runoff are removed). Solid line is the standard deviation of SLH corrected for inverted barometer effects of atmospheric pressure.

for, it might not be necessary to eliminate Astoria from the analysis. In fact, the results of Section 6 show that the residuals of Astoria SLH after river effects have been taken into account are representative of oceanic conditions over these monthly time scales. It is worth noting that the streamflow variations have no significant effect on SLH anomalies at neighboring stations to the north or south.

Since it is the dynamical aspects of SLH variability that are of interest, the second analysis step was to remove the isostatic inverted barometer effects of SLP (1 cm mb^{-1}) from the raw SLH at each of the 20 stations. Because the spatial scales of SLP are large (Davis, 1976), SLP at the FNOC grid point nearest the SLH station was taken to be representative of the local atmospheric pressure at that station. The standard deviations of inverse-barometer-corrected SLH are given in Table 1 and shown as the solid line in Fig. 3. From the ratio of corrected to total variance (Table 1), it can be seen that SLP contributes little to the raw SLH variability south of San Francisco (10–15%). However, to the north the inverted barometer response to SLP accounts for a substantial fraction of the raw SLH variability (50–60%). The discussion that follows deals only with inverse-barometer-corrected SLH (hereafter referred to simply as SLH).

The time and space scales of SLH and SLP can

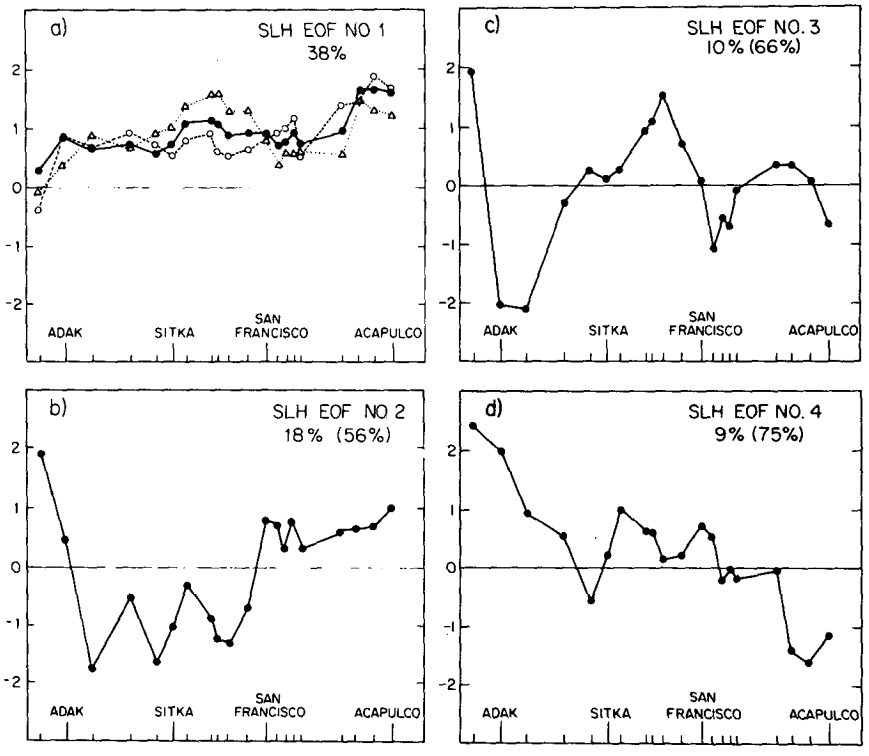

FIG. 4. The four dominant empirical orthogonal functions (EOFs) of anomalous inverse-barometer corrected SLH. The function values have been normalized to have typical value 1 (the sum of their squares is equal to 20, the number of tide stations). The two percentage values correspond to the individual and cumulative percent of SLH variance explained by each pattern. Open circles in (a) represent the dominant EOF of low-frequency (double 13-month running mean) SLH accounting for 49% of the low-frequency variability. Open triangles in (a) represent the dominant EOF of high-frequency SLH (double 13-month running mean subtracted) accounting for 41% of the high-frequency variability.

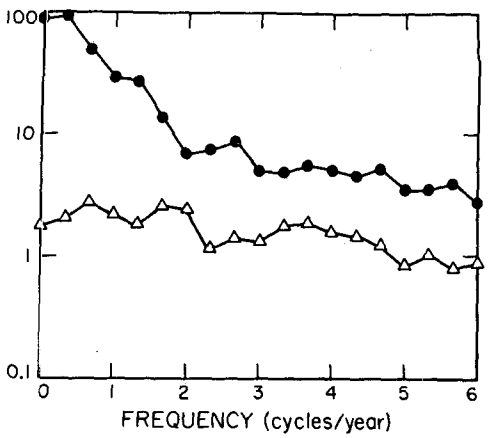

FIG. 5. Frequency spectra of the amplitudes of the first EOF of SLH (solid circles) and SLP (open triangles). Spectral estimates are based on approximately 30 degrees of freedom and units are arbitrary.

be examined by decomposing the data into the dominant spatial empirical orthogonal functions (EOFs) and their time-varying amplitudes. A summary of the essential features of EOFs is given in Davis (1976). The virtues are that 1) they describe the most energetic spatial patterns of variability, and 2) they may be regarded as uncorrelated modes of variability. In this respect EOF analysis is very similar to widely used spectral analysis. In addition, it is often true (as will be shown to be the case in this study in Sections 4 and 5) that some unique physical significance can be ascribed to an individual mode.

The dominant EOFs of SLP over the North Pacific have been described by Davis (1976). Only four patterns are required to explain 90% of the SLP variance. SLH also exhibits very large spatial scales over these monthly time scales. The four most significant patterns, accounting for 75% of the variance over the 20 stations, are given in Table 1 and shown in Fig. 4. The percentages of variance at each of the 20 stations explained by these modes are also given in Table 1. The covariance matrix used to compute the EOFs was constructed from all existing data at each station. The effect of missing data at any station is to reduce the statistical reliability of the covariance estimates somewhat, thereby introducing a small amount of noise in the EOF values. For quasi-stationary time series with sample sizes as large as those examined here, this should be a relatively unimportant effect.

Of particular interest in this study is the dominant mode of variability accounting for 38% of the variance. It indicates that a significant portion of SLH fluctuations consist of a general rise or fall (depending on whether the sign of the time-varying amplitude of the pattern is positive or negative) over the entire region from the Aleutians to Mexico with remarkably constant amplitude over all stations (slightly larger at the three southernmost stations). This pattern of variability will be examined in detail in Section 4. The open circles and triangles in Fig. 4a represent the dominant EOFs of low- and high-pass filtered SLH, respectively. The similarity of these high- and low-frequency EOFs indicates that the principal pattern of variability is relatively independent of frequency.

The principle time scales of variability can be determined by computing the frequency spectra of the amplitude time series of the EOFs. Due to occasional missing SLH data at some of the stations, it was necessary to make an objective estimate of the time amplitude during some months as described in Davis (1976). Because of its simplicity, the expected square error of the estimate of the dominant EOF amplitude never exceeded 8% of the variance of the pattern. The spectra of the first mode of SLH and SLP are shown in Fig. 5. SLH variability is dominated by low-frequency energy (periods > 0.5–1 year), whereas SLP variability shows a more nearly uniform distribution of energy with frequency. The higher order SLH patterns show the same predominance of low-frequency variability. This anticipated result reflects the longer time scales of the ocean relative to the atmosphere.

4. Large-scale variability

Before looking at local (individual station) SLH variability, some aspects of the very large scale variability will be examined. The considerable longshore coherence of the dominant mode of SLH shown in Fig. 4 suggests the importance of some very large scale atmospheric forcing. In a study of SLP/SST connections in the North Pacific, Davis (1978) isolated the principal pattern of SLP most important

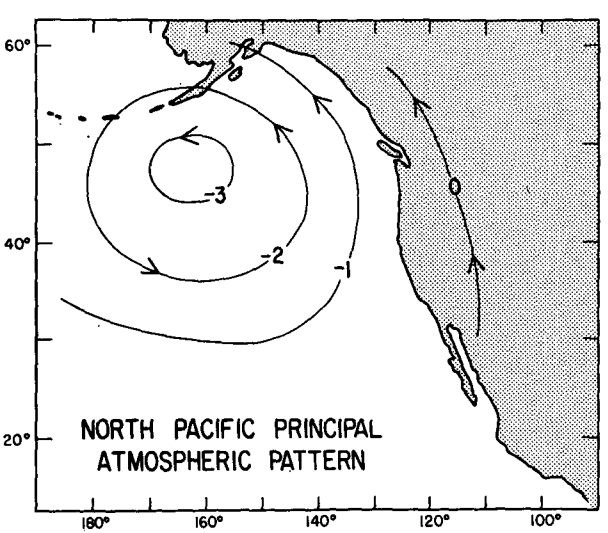

FIG. 6. The principal pattern of North Pacific atmospheric variability (From Davis, 1978).

in causing SST changes in the eastern Pacific. The pattern (Fig. 6) consists of isobars and associated geostrophic winds that sweep around the entire North Pacific. The details of its derivation are not important here but it is useful in this analysis for its description of the very large scale aspects of atmospheric variability. Since SLH gives an integrated measure of upper ocean heat content, a similar strong relationship between the principal atmospheric pattern and the dominant EOF of SLH might be anticipated.

The time-lagged skill in hindcasting the dominant pattern of inverse-barometer-corrected SLH from this basin-wide pattern of atmospheric variability is shown by the solid circles in Fig. 7. A maximum skill of 0.19 (a correlation of 0.44) occurs at zero lag indicating that most of the large-scale response to atmospheric forcing occurs rather rapidly (within a month). This rapid response suggests that the coastal sea-level response to wind forcing is largely barotropic. Although a certain amount of persistence in both SLH and basin-wide atmospheric variability is evident by the significant hindcast skills at both positive and negative one-month lag, the asymmetry in Fig. 7 indicates that there is some dynamic connection between SLH and preceding atmospheric data up to three months in advance (perhaps reflecting the baroclinic part of the sea-level response). The response resembles that expected for anomalous geostrophic currents and associated sea surface slopes induced by basin-wide winds: cyclonic winds result in anomalous poleward currents with SLH rising toward the coast and anticyclonic winds result in anomalous equatorward currents with a corresponding drop in coastal SLH.

To examine the possibility that other large-scale atmospheric variability not accounted for by the principal atmospheric pattern might also be important to variations in the dominant mode of SLH, the time series of the first three EOFs of SLP (see Davis, 1976) were added to the single-input model described above. The resulting increases in estimation skill were small (less than 5% at all lags) with a corresponding artificial skill increase of 1% (because of the increased number of inputs). Thus, nearly all of the large-scale atmospherically forced sea-level variability (after removing the inverse barometric effects of SLP) is driven by the basin-wide pattern in Fig. 6.

Although it is not possible at this point to determine the dynamically important features of the basin-wide principal pressure pattern, dynamical precepts and the inertia of SLH in response to prior forcing suggest that the associated wind stress or wind stress curl is more important than pressure itself. Baroclinic geostrophic adjustment of the density field to applied wind forcing is expected to occur relatively slowly so that during any given month

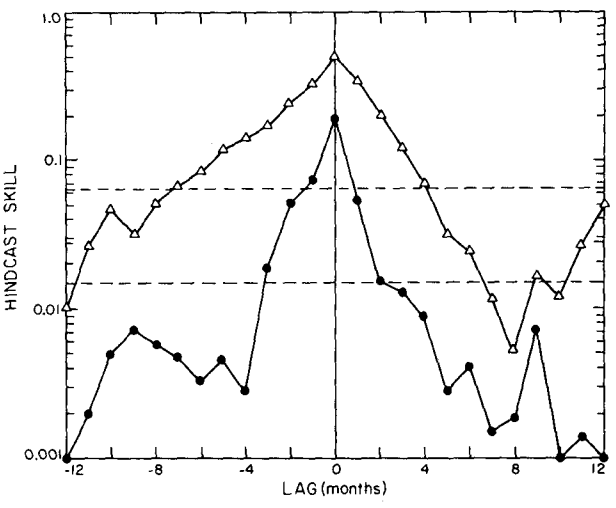

FIG. 7. Skill in estimating the amplitude of the dominant EOF of SLH from the amplitude of the North Pacific principal atmospheric pattern shown in Fig. 6 (solid circles). Lower dashed line is the corresponding 95% significance level. Open triangles represent hindcast skill when eastern tropical Pacific SST (used as an index of El Niño) and the amplitudes of the three dominant EOFs of SLP in the eastern North Pacific are added as inputs and upper dashed line is the corresponding 95% significance level.

there is some residual signal in SLH resulting from flow induced by prior forcing. Since SLH estimation skill from prior atmospheric forcing drops off rapidly at larger lags, it appears that most of the adjustment of the density field occurs within a time scale of around three months. Note that this hypothesis of wind-driven geostrophic currents cannot be quantitatively demonstrated without offshore SLH data to enable measurement of sea surface slope from which geostrophically balanced currents could be inferred. Along the California coastline, Chelton (1980) has shown that coastal SLH anomalies are, in fact, indicative of nearshore geostrophic currents over interannual time scales. However, sampling of historical hydrographic data is not adequate to determine whether this also holds true over shorter time scales.

It is noteworthy that these anomalous currents have a structure quite different from the background currents in the North Pacific. Rather than a cyclonic subpolar gyre and an anticyclonic subtropical gyre, anomalous currents appear to consist of a single basin-wide gyre that fluctuates between cyclonic and anticyclonic flow. This can be interpreted as an indication that, rather than a coherent change in the transport of these two gyres, they fluctuate out of phase. That is, when the poleward transport of the eastern limb of the subpolar gyre increases (decreases), the equatorward transport of the eastern limb of the subtropical gyre decreases (increases). This behavior could arise, for example, from a quasi-permanent transport of the West Wind Drift in the central North Pacific which bifurcates in the eastern

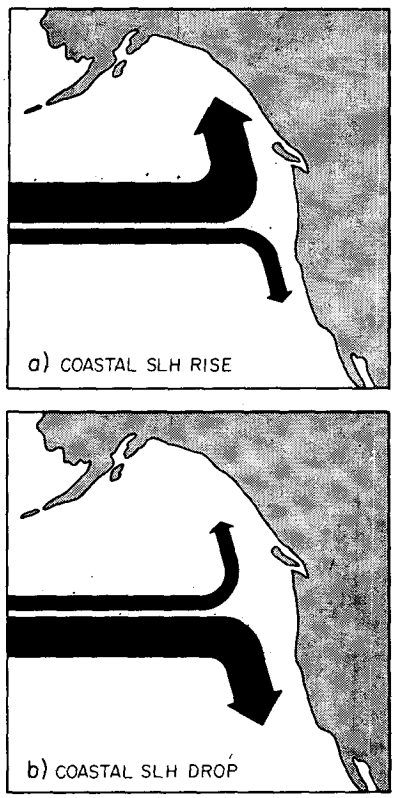

FIG. 8. Schematic picture of the eastern Pacific bifurcation of the West Wind Drift suggested by the first EOF of anomalous SLH. Positive SLH anomalies correspond to (a) and negative SLH anomalies to (b).

North Pacific either with most of the transport turning northward or most of the transport turning southward. These two cases are shown schematically in Fig. 8. Fig. 7 indicates that 20% of these anomalous current fluctuations are driven by basin-wide wind forcing. Perhaps part of the remainder of these large-scale variations is related to instabilities in the eastern extension of the mid-latitude jet.

Note that from SLH measurements only at the coast it is impossible to determine whether the geostrophic flow along the eastern boundary is indeed part of a basin-wide anomalous current as hypothesized above. In fact, a rapid (barotropic) basin-wide response is difficult to justify dynamically; a barotropic response trapped on the shelf seems more likely. This type of response would be driven by longshore winds over the shelf. However, it will be shown in Section 6 (model M_2) that the coastal sea-level response is more closely coupled to basin-wide winds than to local winds over the shelf. This supports the hypothesis that the large-scale coastal SLH variations are part of a basin-wide anomalous current system.

Some additional insight into the large-scale SLH response can be gained by looking at the hindcast skill as a function of frequency. This is given by the squared multiple coherence (see Bendat and Piersol, 1971; Chelton, 1980, Appendix B). The boxes in Fig. 9 represent the frequency-dependent skill in estimating the first EOF of SLH from the basin-wide atmospheric pattern alone. For comparison, the solid circles represent the estimation skill when the three dominant EOFs of SLP are added to the model. It can be seen that, although small, the primary contribution of these three SLP patterns to the hindcast skill occurs at frequencies > 2 cycles per year (cpy). The resulting estimation skill is more or less uniform (35–50%) over all frequencies.

The residual spectrum after removing the effects of the four atmospheric parameters on the dominant EOF of SLH is shown by the solid dots in Fig. 10. A significant amount of large-scale SLH variability over interannual time scales remains unexplainable in terms of atmospheric forcing. Enfield and Allen (1980) have suggested that this low-frequency variability is related to El Niño phenomena in the eastern tropical Pacific. The interannual aspects of large-scale SLH variability can be isolated by computing double 13-month running mean of SLH at each individual station (see Appendix). The standard deviations of the resulting low-pass filtered SLH are given in Table 2 along with the ratio of low-frequency to total variance at each station. Variability at frequencies < 1 cpy typically accounts for 15–20% of the total variance from Unalaska to Avila Beach and 30–40% of the total variance at stations farther south

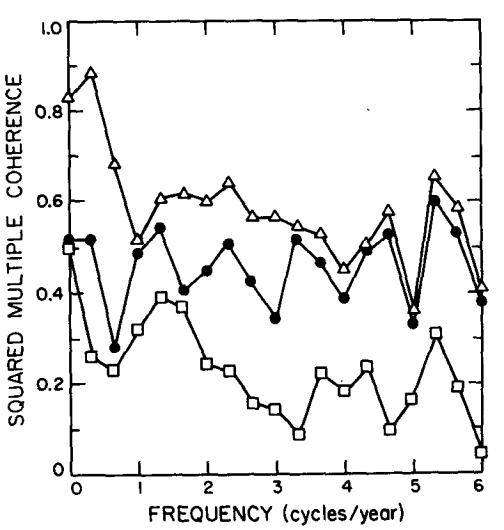

FIG. 9. Skill in estimating the amplitude of the first EOF of inverse-barometer-corrected SLH as a function of frequency (the squared multiple coherence). Open squares represent skill from the principle atmospheric pattern alone. Solid circles represent skill after addition of the three dominant EOFs of SLP in the eastern North Pacific. Open triangles correspond to skill after addition of eastern tropical Pacific SST (an index of El Niño). Spectral estimates used to compute the squared coherence values are based on approximately 30 degrees of freedom.

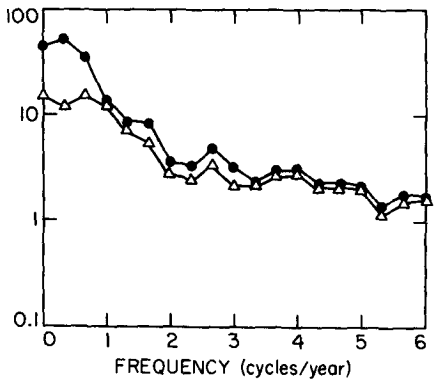

FIG. 10. Spectra of residual SLH after removing effects of the principal atmospheric pattern and the three dominant EOFs of SLP (solid circles) and after also removing the effects of eastern tropical Pacific SST (open triangles). Spectral estimates are based on approximately 30 degrees of freedom.

and at Attu and Adak. The dominant EOF of this low-frequency SLH is given in Table 2 and shown by the open circles in Fig. 4a. The pattern rather closely resembles the dominant EOF of unfiltered SLH. The percentages of low-frequency and total SLH variance accounted for at each individual station by this mode of variability are also given in Table 2. This pattern accounts for a very large fraction of the low-frequency variance at all stations except Attu (especially at stations south of San Francisco). The unusually high percentage of low-frequency variance explained at Kodiak should be interpreted with caution because of the short record length at that station (see Table 1 and Fig. 2).

The amplitude time series of the dominant EOF of low-frequency SLH is shown by the solid line in Fig. 11. For comparison, the dashed line in the figure represents a double 13-month running mean of sea surface temperature (SST) averaged over a region from the equator to 10°S and from the coast of South America to 100°W. SST in this region is generally considered to be an index of El Niño (Allison *et al.*, 1972). Definitions of El Niño vary but it is usually associated with a rapid appearance of warm water off the coast of Peru and southern Ecuador (hence the use of SST rather than SLH as an indicator of El Niño). The major El Niño events of 1957–58, 1965, 1969–70 and 1972–73 generally cited in the literature (e.g., Wyrtki, 1975) are clearly evident in both eastern tropical Pacific SST and west coast SLH as well as a number of the more minor events. The correlation between these two time series is 0.73. Positive SST and SLH anomalies indicate El Niño periods, while negative anomalies represent "anti-El Niño" periods. This is rather conclusive evidence that El Niño cannot be considered a local event restricted to the eastern tropical Pacific or even the equatorial Pacific. Related effects can be seen everywhere along the eastern rim of the North Pacific. The El Niño signal in SLH at any individual station is often masked by the large response to other factors (particularly at the higher latitude stations) but EOF analysis has succeeded in extracting this process from the "noise" at each station.

The resulting time-lagged hindcast skill after adding the El Niño index to the four input model described above is shown by the open triangles in Fig. 7. The estimation skill at zero lag increases to 0.5 (a multiple correlation of 0.71). The squared multiple coherence (see the open triangles in Fig. 9) indicates that nearly all of this increased estimation skill is in the interannual frequency band (hence the high persistence evident in the time-lagged hindcast skill in Fig. 7). Approximately 70–80% of the variance between 0 and 1 cpy is explained by the El Niño index and the four atmospheric parameters.

As pointed out in the Introduction, the presence of El Niño related effects at these mid-latitudes has been suggested analytically and numerically by the models of Godfrey (1975), McCreary (1976) and Hurlburt *et al.* (1976). These models indicate that El Niño events originate in the tropics from anomalous forcing by the trade winds and propagate poleward along the eastern boundary of the Pacific as coastal Kelvin waves. EOF analysis is designed to describe only simultaneous covariability between all stations (standing wave phenomena) and therefore

TABLE 2. Statistical characteristics of low-frequency (double 13-month running mean) SLH at each of the 20 individual stations: σ_L is the standard deviation of the low-pass filtered SLH and σ_L^2/σ_T^2 the ratio of low-pass filtered to total SLH variance (corrected for inverse barometric effects). Also given are the values of the principal EOF of low-pass filtered SLH (accounting for 49% of the overall low-frequency SLH variance) and the percentages of low-pass filtered and total variance explained at each individual station by the principal EOF of low frequency SLH. Sea-level records were detrended and inverse barometer corrected.

Station	σ_L (cm)	σ_L^2/σ_T^2	EOF No. 1 (49%)	σ_L^2 (percent)	σ_T^2 (percent)
Attu	4.0	0.33	−0.40	3	1
Adak	3.5	0.40	0.82	17	7
Unalaska	2.7	0.20	0.62	16	5
Kodiak	1.8	0.26	0.92	90	23
Yakutat	2.4	0.20	0.73	29	6
Sitka	1.8	0.21	0.52	26	6
Prince Rupert	2.3	0.19	0.79	50	8
Tofino	1.9	0.15	0.90	75	11
Neah Bay	1.8	0.12	0.61	39	4
Astoria	2.5	0.19	0.56	17	3
Crescent City	1.7	0.13	0.65	46	6
San Francisco	2.0	0.20	0.89	63	13
Avila Beach	2.0	0.23	0.94	73	17
Los Angeles	2.0	0.36	0.99	78	28
San Diego	2.2	0.34	1.19	92	31
Ensenada	1.2	0.14	0.51	56	8
La Paz	2.5	0.39	1.39	98	38
Mazatlan	3.3	0.29	1.44	60	18
Manzanillo	3.7	0.36	1.88	84	30
Acapulco	3.6	0.30	1.66	68	21

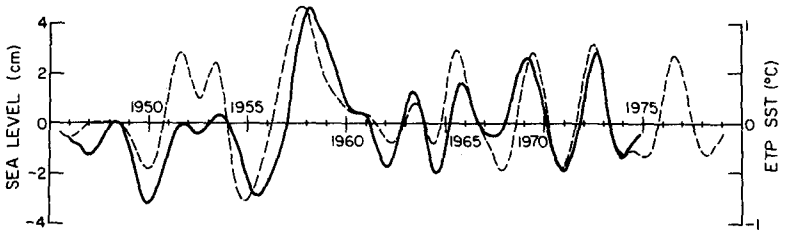

FIG. 11. Time series of low-frequency (double 13-month running mean) eastern tropical Pacific SST (dashed line) and the amplitude of the dominant pattern of low-frequency SLH (solid line). Tic marks are January and year labels are centered at January of that year. The value of sea level (cm) in a given month at a particular location is determined by multiplying the time amplitude for that month by the spatial EOF value as given in Table 2 for that station.

cannot detect any time-lagged propagation between stations. If the wavelength of these coastally trapped waves are long enough, SLH fluctuations associated with this wave would essentially appear simultaneously at all 20 stations. The amplitude-time series in Fig. 11 thus describes the average time of occurrence of the El Niño signal over all 20 SLH stations. With the exception of the 1968–69 event, it can be seen from Fig. 11 that eastern tropical Pacific SST leads the first EOF of SLH during all major El Niño and anti-El Niño occurrences, making poleward propagation a plausible mechanism.

As a more quantitative test of the propagation theory the time-lagged correlation between eastern tropical Pacific SST and low-frequency SLH (0.125–1 cpy) at each of the 20 individual stations was computed. The method used to filter the SLH data is described in the Appendix. The contoured correlations in Fig. 12 indicate a definitive asymmetry in the correlation with SST leading SLH. The amount by which SST leads SLH increases in a fairly systematic manner with increasing distance along the coastline. The El Niño signal in eastern tropical Pacific SST occurs nearly simultaneously with Acapulco SLH but appears to lead San Francisco SLH by about 4 months. For reference, the dashed line in the figure corresponds to a poleward phase speed of 40 cm s^{-1} (~35 km day^{-1}). Enfield and Allen (1980) also present evidence for poleward propagation of low-frequency SLH anomalies (the same frequencies extracted by the filter used here) using a different analysis technique. They find a somewhat

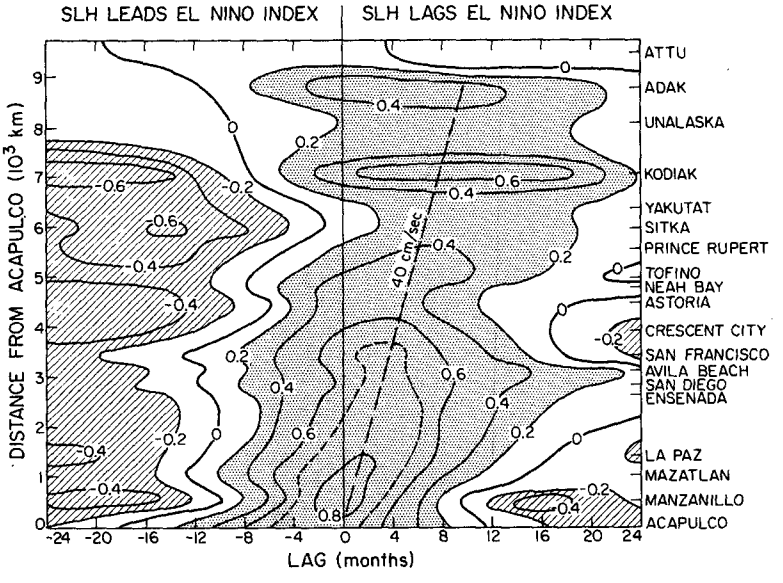

FIG. 12. Contour plot of the correlation between low-frequency SLH in month (t + lag) at each of the 20 tide-gauge stations and low-frequency eastern tropical Pacific SST in month t. Shaded region corresponds to correlation values > 0.2 and hatched regions correspond to correlation values < −0.2. Dashed line represents approximately 40 cm s^{-1} northward propagation. The 95% significance level corresponds to correlations of ~0.35.

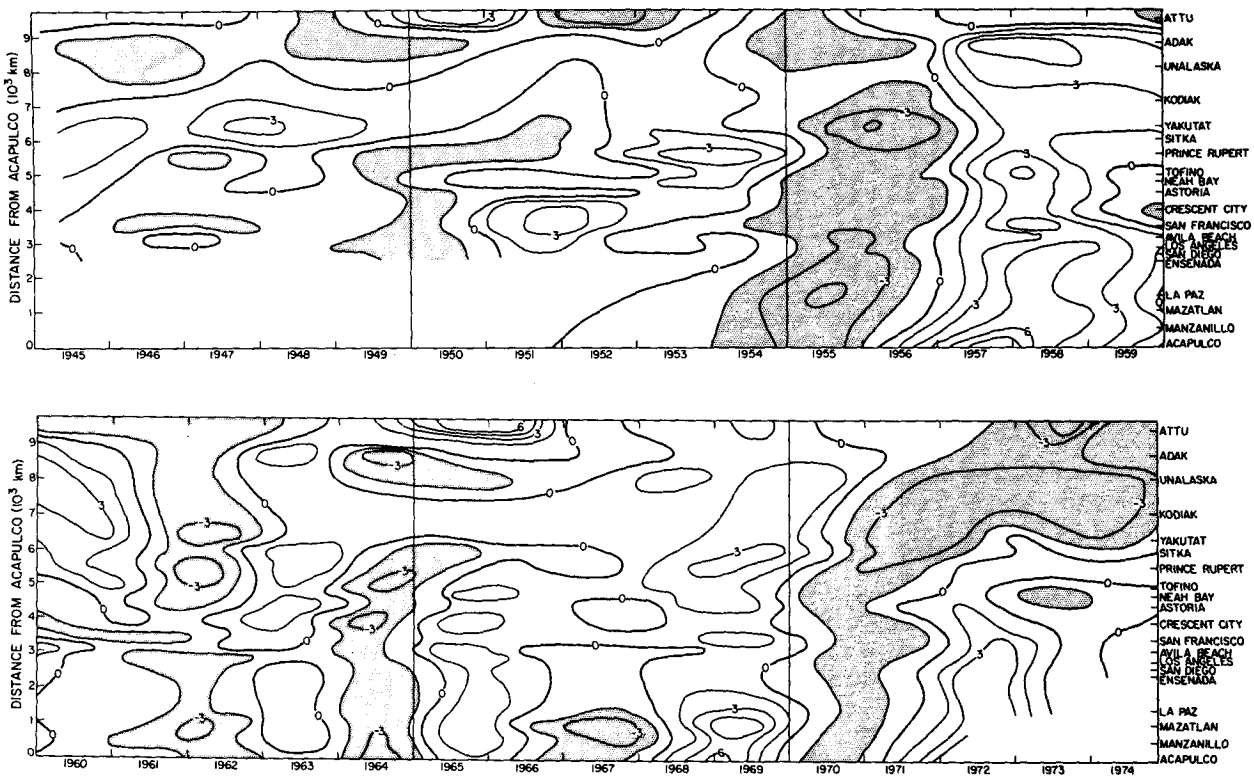

FIG. 13. Contour plot of low-frequency SLH anomalies from Attu to Acapulco for the 30-year time period 1945–74. Shaded regions represent SLH anomalies < -1.5 cm. Method of filtering is described in the text.

more rapid phase speed of about 75 km day^{-1} and suggest that penetration of El Niño related events poleward of San Francisco is weak. The relation of these low-frequency SLH variations to El Niño is shown somewhat more simply here in Fig. 12 which also shows the presence of the El Niño signal as far north as Adak (although the correlations are only marginally significant poleward of Price Rupert). It is interesting that low-frequency SLH variability at Attu appears to be unrelated to El Niño. (Note also from Fig. 4a and Table 2 that the first EOF of low-frequency SLH contributes little to the variability at Attu.)

It is useful to depart from a statistical description of the relation between El Niño and west coast SLH and examine individual events in some detail. SLH anomalies in the 0.125–1 cpy frequency band (see Appendix) are contoured in Fig. 13. The independent behavior of SLH at Attu is very clearly seen. A lack of any pronounced El Niño or anti-El Niño related events anywhere along the west coast prior to 1952 is also evident. However, over the rest of the record, there is a definite tendency for large-scale events to propagate poleward. Interestingly, the statistical relation in Fig. 12 appears to reflect the effects of negative, somewhat more so than positive, SLH anomalies. This is especially true of the 1954–55 and 1970 events which clearly propagate all the way from Acapulco northward to Alaska. In comparison, the positive SLH anomalies can be seen to propagate from Acapulco to San Francisco but they frequently either do not propagate any farther poleward (e.g., 1965–66 and 1971–73) or their occurrence is nearly simultaneous over all stations from San Francisco to Adak (e.g., 1957–59). This simultaneous occurrence of the 1957–59 positive SLH anomaly poleward of San Francisco probably reflects the co-occurrence of anticyclonic basin-wide winds over the North Pacific noted by Namias (1976). However, Fig. 13 indicates that the co-occurrence of this large-scale atmospheric variability with El Niño is apparently not a regular occurrence.

One thing that is clear from Fig. 13 is that, although there may be an underlying tendency for SLH anomalies to propagate poleward, there is also a large amount of inherent low-frequency variability that is either unrelated to poleward propagation or propagates too rapidly to be detected in monthly averages. This is also clearly shown by the open triangles in Fig. 10 which represent the residual SLH spectrum after removing the effects of El Niño and the four atmospheric parameters on the dominant EOF of SLH. Although much of the low-frequency, large-scale SLH variability is related to El Niño-type events, there is still a significant amount of residual SLH variability at frequencies < 2 cpy.

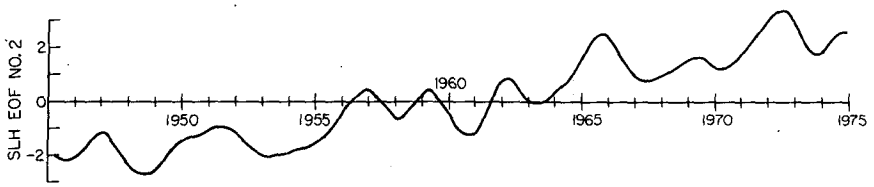

FIG. 14. Amplitude-time series of the second EOF of SLH shown in Fig. 4b smoothed by a double 13-month running mean.

5. Secular variability

The physical significance of the second EOF of SLH (Fig. 4b) becomes clear from the plot of the corresponding amplitude-time series, smoothed by a double 13-month running mean, in Fig. 14. It represents a secular trend in SLH over the full 29-year-record length. The spatial distribution of the pattern indicates that the trend is not regular or the same at all locations and, in fact, differs in sign from one region to another. Fig. 4b suggests that SLH has been rising at all stations from San Francisco southward and at the Aleutian Island stations where the sign of the spatial pattern is positive. In comparison, SLH appears to have been generally falling from Unalaska to Crescent City where the sign of the pattern is negative.

The effectiveness of the EOF technique in extracting this physical mode of variability can be demonstrated by least-squares fitting the SLH data at each individual station to a linear trend. The resulting rates of SLH rise/fall over the observed 29-year period are given in Table 1 and are shown by the solid circles in Fig. 15. Note the close similarity to the spatial distribution of the EOF reproduced as the open circles in the figure.

These trends are visually evident in Fig. 2. They have been previously noted by Hicks and Shofnos (1965) and Roden (1966). Trends in tide-gauge measured sea-level records can result either from actual changes in the water level or from slow vertical movement of the tide gauge with respect to a geoid. Hicks (1978) has shown that over the Atlantic, Gulf of Mexico and southern Pacific coasts of the United States, SLH has generally been rising over the last four decades. This is attributed by geologists to the glacial eustatic rise in sea level resulting from an increase in the water volume of the oceans from melting glaciers. Hicks (1978) estimates a eustatic SLH rise of about 0.15 cm year^{-1} since 1940.

In contrast to the rising SLH observed over most of the world ocean, SLH has been falling along the southeastern coast of Alaska, in Scandinavia and in the Hudson Bay region (Gutenberg, 1941). This is generally thought to be due to an uplift of the land in these regions as a result of isostatic rebound of the earth's crust from the most recent glaciation, rather than a true sea-level change. The land emergence in southeastern Alaska is believed to be centered near Glacier Bay, located between Yakutat and Sitka, and Hicks and Shofnos (1965) have estimated a 0.4 cm year^{-1} rate of uplift from SLH records. This amounts to about twice the rate of uplift inferred from SLH records in the Hudson Bay region.

A similar drop in SLH has been observed along the coast of Japan and has been attributed to emergence of the Japanese land mass from tectonic processes (Tsumura, 1970). However, White *et al.* (1979) have proposed another mechanism for the observed drop in coastal SLH. From the vertical distribution of temperature and salinity they have shown that computed steric sea level over the entire western North Pacific has decreased 2–4 cm over the period from 1954–72 due to a reduction of heat content of the upper ocean.

A continuous record of upper ocean hydrographic data is not available in the northeastern Pacific for computing a time series of steric sea level. However, examination of SST records in this region suggests a similar decrease in upper ocean heat content. Fig. 16 is a double 37-month running mean of 5° average SST centered at 55°N, 140°W in the northeast Pacific. It reveals a 4°C decrease in SST since about 1958. So it appears that the reduction of upper ocean heat content observed by White *et al.* (1979) in the western Pacific has been occurring in the northeastern Pacific as well.

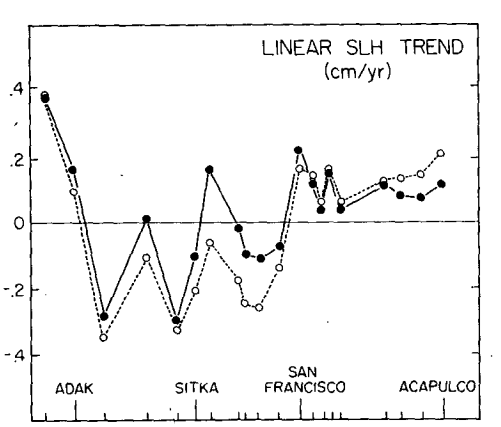

FIG. 15. Rate of linear SLH trend (cm year^{-1}) as determined by a least-squares regression of a straight line to the 30 years of data at each tide-gauge station (solid circles). The second EOF of SLH shown in Fig. 4b is reproduced here as the open circles.

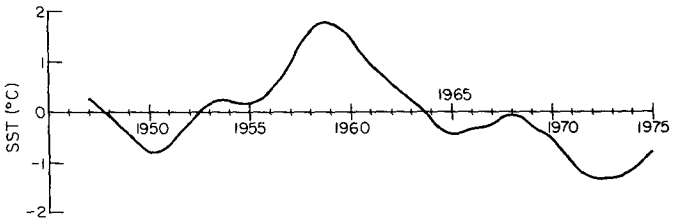

FIG. 16. Double 37-month running mean of 5° average sea surface temperature in the northeast Pacific centered at 55°N, 140°W (near Yakutat, Alaska).

This presents some interesting suggestions about the cause of observed SLH trends at the high-latitude stations. Without subsurface temperature measurements to compute the integrated effect of this decrease in upper ocean heat content, it is not possible to evaluate the relative importance of thermal effects versus isostatic rebound in causing the observed drop in SLH in the northeastern Pacific. However, if the observed 4°C decrease in water temperature at the surface extended to a mixed layer depth of 65 m (not unreasonable), the resulting drop in SLH would be one-half that measured at Yakutat. A 4°C temperature drop in the upper 130 m would account for all of the measured SLH drop at Yakutat. Thus, at least from 1958, a significant portion of the secular drop in tide-gauge measured SLH may reflect a true sea-level change rather than purely isostatic rebound. It must be stressed that the statistical reliability of any speculations about the cause of trends is necessarily low since they effectively represent less than one complete realization of the process. The implications will not be pursued further here except to point out that estimates of the viscosity of the earth's upper crust computed from SLH trends in this region must be considered to be a lower bound on the true value (e.g., Crittenden, 1967; Clark, 1977).

As pointed out earlier in Section 2, because these low-frequency aspects of variability are not well sampled by the short records, they lead to sampling errors which increase the artificial predictability of SLH. Hence, the linear trends in Table 1 and Fig. 15 were removed from the SLH time series at each station before formulating the linear statistical models described in Section 6. It is worth noting that no significant secular variability is evident in any of the atmospheric data examined in this study.

6. Local variability

In addition to the large-scale response examined in Section 4, part of the variability of SLH at each station is expected to reflect local forcing. The important inputs for a statistical model of SLH variability can be determined from the linear dynamical model derived by Clarke (1977) which includes the effects of both stratification and bottom topography. Consider an eastern boundary with the coastline along the y-axis (pointed northward). Define p to be the perturbation pressure from a state of rest divided by $\rho_0 g$, where ρ_0 is a representative density of the water and g the gravitational acceleration. The expression for p reduces to an eigenvalue problem and the eigenfunctions $F_n(x, z)$ form a complete set. Then p can be expressed in terms of a sum of modes

$$p(x, y, z, t) = \sum_{n=0}^{\infty} F_n(x, z) h_n(y, t).$$

Clarke (1977) shows that the solution for the y, t dependence of the pressure of each mode satisifes the forced, first-order wave equation

$$\frac{1}{c_n}\frac{\partial h_n}{\partial t} + \frac{\partial h_n}{\partial y} = \frac{q_n \tau^y}{\rho_0 g H}, \tag{1}$$

where c_n is the eigenvalue, q_n a constant pertaining to mode n, H the mixed layer depth and τ^y the longshore (poleward) component of local wind stress. Implicit in (1) are the assumptions that 1) the time scales of interest are much longer than an inertial period, 2) the cross-shore scale of variability is much smaller than the longshore scale; 3) the longshore wind stress at the coast is much more efficient at generating vorticity over the shelf than either atmospheric pressure or the wind-stress curl, and 4) effects of dissipation can be neglected. (The validity of this last assumption is somewhat questionable.) Free solutions to (1) are of the form $\phi(y - c_n t)$ which represent long-wavelength "coastal trapped waves" (a hybrid of continental shelf waves and internal Kelvin waves) that propagate poleward with phase speed c_n. Note that at low enough frequencies the coastal trapping of wave energy is no longer valid. McCreary (1977) and Cane and Sarachik (1977) show that there is a "critical latitude" below which the coastal trapped wave energy "leaks" offshore in the form of westward-propagating Rossby waves; the critical latitude increases with decreasing wave frequency. However, the response at the coast still has the characteristics described by (1).

The forcing parameters relevant to a statistical model can be found by looking at two limiting cases of (1). The first is the "short-time" solution,

$$\frac{\partial h_n}{\partial t} = a_n \tau^y, \tag{2}$$

where a_n is a constant. Physically, a poleward wind stress forces an onshore Ekman transport which results in a convergence of water at the coast. SLH rises and, in order to conserve mass, there is downwelling and a compensating offshore geostrophic flow in the deep water [see Eq. (3)]. Then (2) suggests $\int_{t_0}^{t} \tau^y dt'$ as an important input in the statistical model for estimating SLH. The white spectra of monthly averages of atmospheric variability (see Fig. 5) and the rapid response of coastal SLH to wind forcing demonstrated from more closely sampled data (e.g., Smith, 1974) suggest a very short memory of SLH at any individual station to past wind forcing. So, in the statistical models to be examined here, the integral will be taken only over the same month over which SLH is averaged, i.e., monthly mean SLH will be estimated from concurrent monthly mean wind stress. (Extending the integral to include the preceding month did not significantly increase the estimation skill.)

The time rate of change of SLH described by the "short time" solution (2) does not continue indefinitely. A longshore tilt begins to develop and the "long-time" solution is

$$\frac{\partial h_n}{\partial y} = b_n \tau^y, \tag{3}$$

where b_n is a constant. Wind-forced coastal trapped waves described by the full equation (1) carry out the transient adjustment to attain the steady-state solution (3). For poleward wind stress, the resulting south-to-north rise in SLH is associated with an offshore geostrophic transport that exactly balances the wind-driven onshore Ekman transport. There are two aspects of this dynamical balance that can be examined statistically. The first is to note that (3) can be integrated from the adjacent station to the south (separated by a distance L_y) to get

$$h_n(y) = h_n(y - L_y) + b_n L_y \bar{\tau}^y, \tag{4}$$

where $\bar{\tau}^y$ is the average longshore wind stress between the two stations. Eq. (4) shows that SLH at the adjacent station to the south and the average wind stress between the two stations are two additional inputs relevant to a statistical model for SLH variability. Note that since the spatial scales of atmospheric variability are large, $\bar{\tau}^y$ would not be expected to differ greatly from τ^y for moderate L_y. Indeed, for the SLH stations examined here, the correlations between longshore wind stress at neighboring stations were typically between 0.8 and 0.9.

A significant hindcast skill in the estimation of $h_n(y)$ by a statistical model analogous to (4) is not necessarily indicative of the importance of locally generated wind-forced coastal trapped waves. The longshore wind stress could be zero and, because of the assumption of long-wavelength solutions inherent in (1), a significant estimation skill in the statistical model could result from a strong relation between SLH at neighboring stations due to the presence of freely propagating waves. Therefore, the second aspect of (3) to be examined statistically is given by

$$\Delta h = h_n(y) - h_n(y - L_y) = b_n L_y \bar{\tau}^y. \tag{5}$$

A significant estimation skill in both of the statistical models analogous to (4) and (5) would reflect the importance of locally forced coastal trapped waves in adjusting the system to the steady-state balance (3).

In summary, the discussion above suggests that longshore wind stress and SLH at the adjacent station to the south are the relevant forcing parameters to be included in a statistical model for SLH variability. It must be emphasized that, since all atmospheric parameters are correlated, isolating any single dynamical model to be investigated by an equivalent statistical model can always be misleading. A strong statistical relation might be found, even if the selected forcing parameters are not themselves responsible for the SLH variability. As examples, suppose either the response of SLH to local atmospheric pressure were non-isostatic, or that the response to onshore wind stress were nonzero. Then, since longshore wind stress is correlated with both of these parameters, part of the SLH response would be falsely attributed to longshore wind stress if pressure and onshore wind stress were not included in the statistical model. Therefore, all three of these atmospheric parameters will be included in the statistical models examined in this study. If local pressure and onshore wind stress do not force SLH variations, the discussion in Chelton (1982) shows that their response coefficients in the statistical model will be zero.

In order to sort out the relative importance of the dynamical balances suggested by (2) and (3), a hierarchy of statistical models of the form described in Section 2 will be examined at each individual station. The first and simplest consists of:

MODEL M_1

$d_1(t)$ = local atmospheric pressure
$d_2(t)$ = local longshore wind stress
$d_3(t)$ = local onshore wind stress.

The results are summarized in Table 3 and shown in Figs. 17 and 18. Since the spatial scales of atmospheric variability are large (see Davis, 1976), pressure and wind stress at the FNOC grid point nearest the SLH station were taken to be representative of the local variability at that station. This seemed preferable to interpolation to the SLH sta-

TABLE 3. Hindcast skills, 95% significance levels (in parentheses) and response coefficients for model M_1 (see text). Angles of coastline used to compute wind stress components in this study are also given (measured clockwise from due north). Error bars on response coefficients correspond to 90% confidence limits.

Station	S_H	β_1 (cm mb^{-1})	β_2 (cm^3 dyn^{-1})	β_3 (cm^3 dyn^{-1})	Angle of coastline
Attu	0.03 (0.035)	0.18 ± 0.19	−0.05 ± 1.74	−0.47 ± 1.20	293°
Adak	0.06 (0.041)	0.10 ± 0.16	1.58 ± 1.65	−1.12 ± 1.66	263°
Unalaska	0.15 (0.031)	−0.12 ± 0.13	2.55 ± 1.40	−1.48 ± 1.59	239°
Kodiak	0.12 (0.037)	−0.15 ± 0.12	1.44 ± 1.24	0.16 ± 0.88	235°
Yakutat	0.22 (0.031)	−0.27 ± 0.16	2.10 ± 1.62	1.89 ± 1.58	296°
Sitka	0.19 (0.036)	−0.20 ± 0.17	2.08 ± 1.38	−0.24 ± 1.47	334°
Prince Rupert	0.22 (0.028)	−0.36 ± 0.23	2.40 ± 1.68	−0.37 ± 1.65	334°
Tofino	0.39 (0.027)	−0.63 ± 0.25	3.36 ± 2.17	0.35 ± 1.82	308°
Neah Bay	0.43 (0.025)	−0.80 ± 0.25	2.16 ± 1.71	−0.63 ± 2.28	342°
Astoria	0.34 (0.027)	−0.61 ± 0.34	3.49 ± 2.16	4.68 ± 2.77	0°
Crescent City	0.37 (0.028)	−0.71 ± 0.38	3.19 ± 1.55	−1.73 ± 2.78	4°
San Francisco	0.24 (0.040)	−0.87 ± 0.48	2.21 ± 2.42	−1.48 ± 3.41	329°
Avila Beach	0.03 (0.030)	−0.43 ± 0.53	1.66 ± 2.58	−2.55 ± 3.28	329°
Los Angeles	0.03 (0.021)	−0.58 ± 0.46	1.18 ± 2.66	−1.77 ± 2.99	300°
San Diego	0.05 (0.029)	−0.57 ± 0.55	0.83 ± 2.56	−4.11 ± 4.13	336°
Ensenada	0.05 (0.037)	−0.70 ± 0.58	−0.01 ± 2.76	1.75 ± 5.01	336°
La Paz	0.05 (0.128)	−0.97 ± 1.53	0.79 ± 8.75	−5.47 ± 14.60	311°
Mazatlan	0.13 (0.093)	−1.47 ± 1.99	9.18 ± 11.10	−1.52 ± 15.71	319°
Manzanillo	0.08 (0.105)	−1.76 ± 2.34	5.07 ± 15.34	−5.41 ± 16.57	305°
Acapulco	0.08 (0.059)	−2.01 ± 1.69	7.16 ± 9.27	11.45 ± 13.91	292°

tion which would require the use of (questionable quality) atmospheric data over land. In no cases did the FNOC grid point lie more than 200 km from the SLH station and, in most cases, it was within 100 km. These separation distances are believed to be non-significant in view of the fact that the FNOC quasi-geostrophic winds are computed by an atmospheric pressure differencing scheme which effectively limits spatial resolution to about 500 km at 30°N and 750 km at 60°N. Clearly, the FNOC winds are only representative of the very large spatial scales of variability. Longshore and onshore directions were defined rather arbitrarily at each station by the general visual trend of the coastline in the vicinity of the tide gauge (see Table 3).

The skill in hindcasting SLH at each of the 20 stations from concurrent forcing using Model M_1 is shown in Fig. 17. The estimation skill is significant only from Unalaska to San Francisco, with model M_1 accounting for between 15 and 40% of the variance.

The spatial distributions of each of the response coefficients in Model M_1 are shown in Fig. 18. The shaded areas correspond approximately to the 90% confidence regions about the sample estimates: there is 5% probability that the true value of the response coefficients exceed the upper bound and 5% probability that the true values are less than the lower bound of the confidence region. The rather large ranges of expected variability illustrate the difficulty in accurately estimating the dynamical response coefficients in complex systems. As discussed in Section 2, this difficulty is enhanced when the input time series are inter-correlated. The only way to estimate the response coefficients more accurately is to increase the record length. The erratic behavior and greater uncertainty of the response coefficients at the Mexican stations are primarily due to the lower estimation skill from the statistical model at these stations (see Section 2). The predominance of low-frequency energy and shorter record lengths (both of which reduce the effective number of degrees of freedom) also contribute to the larger error bars at the Mexican stations.

The response to local wind shows that the longshore wind stress does, in general, force a larger SLH response than the onshore component. The response is consistent with simple notions of Ekman dynamics along a coastline. That is, equatorward winds lead to an offshore water transport and a drop in coastal SLH (the classical picture of coastal upwelling). With the exception of Astoria (corrected for river

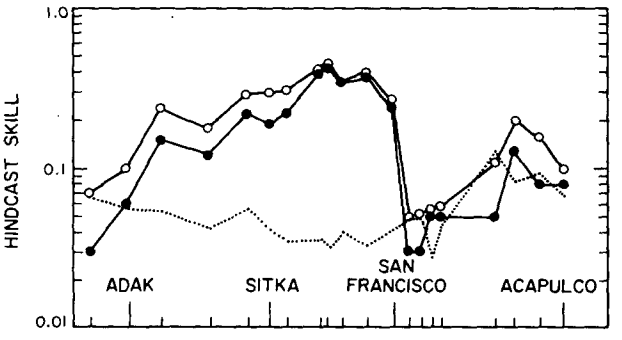

FIG. 17. Skill in estimating SLH at each station from model M_1 (solid circles) and model M_2 (open circles). Dotted line corresponds to the 95% significance level for the hindcast skills of model M_2.

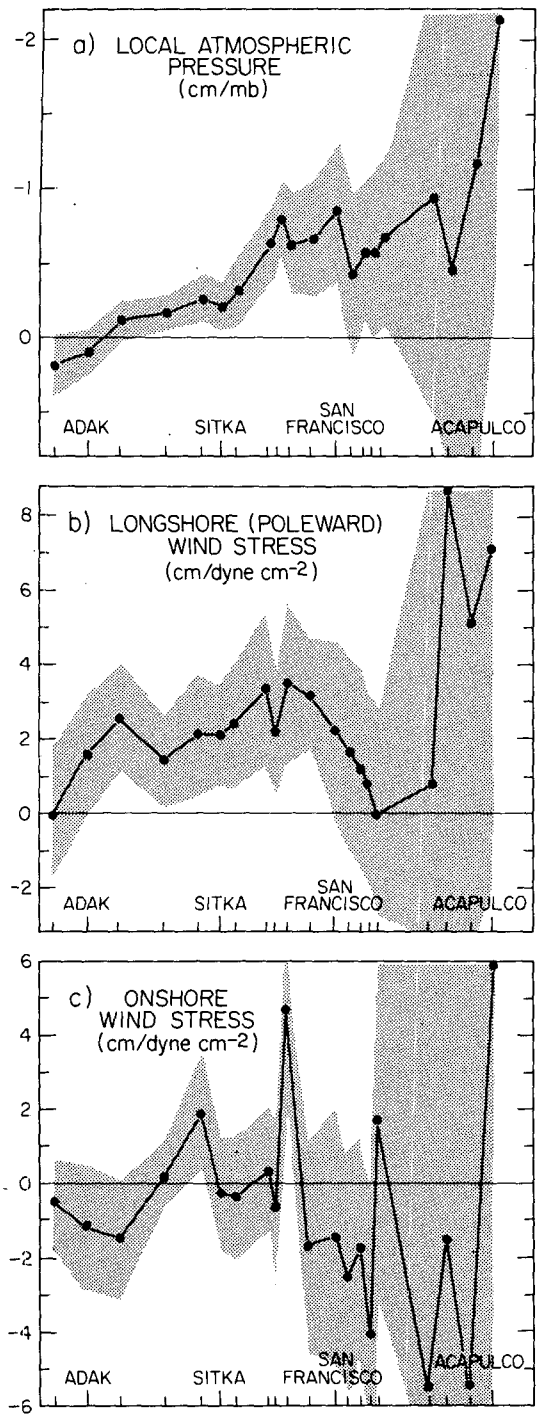

FIG. 18. Spatial distribution of the response coefficients of model M_1. Shaded areas correspond to the approximate 90% confidence region about the sample estimates (computed as described in Section 2). There is 5% probability that the true value of the response coefficient exceeds the upper bound and 5% probability that the true value is less than the lower bound of the confidence region.

effects) and, to a lesser extent, Yakutat, where onshore winds lead to a considerable rise in SLH, the response to onshore wind stress is generally small. The Astoria tide gauge is located in the mouth of the Columbia River and the Yakutat tide gauge is located inside a large bay. The large response to onshore winds at these two locations could be an indication of the importance of wind set-up in semi-enclosed basins.

Perhaps the most interesting feature in Fig. 18 is that the response of SLH to local atmospheric pressure is not inverse barometric at all locations as expected from simple theoretical considerations. The response is significantly larger than inverse barometric from Yakutat to San Francisco with a value 60–80% greater than the theoretical value from Tofino to San Francisco. The expected zero response of inverse-barometer-corrected SLH to local pressure does not even fall within the 99% confidence region about the estimated value in this region.

Since both pressure and wind stress have been included in the statistical model, the results above indicate that the non-barometric response of SLH is apparently not due to effects of local wind stress (as represented by the FNOC winds) as suggested by Saur (1962). There must be some other reason for the greater than inverse barometric response. The most obvious explanation is that pressure may be correlated with some other variable that has not been included in the statistical model. In Section 4 it was demonstrated that part of the SLH at each station appears to reflect basin-wide scales of anomalous geostrophic flow forced by very large-scale winds. In addition to determining whether the non-barometric response can be attributed to the effect of these basin-wide winds, it is useful to examine the relationship between basin-wide and local winds along the coastline. The two aspects of the wind field are found to be strongly related (correlations from 0.5 to 0.65) from Unalaska to San Francisco so the apparent response of SLH to local longshore wind stress shown in Fig. 18 may just reflect a response to basin-wide winds. The true effect of each parameter can be examined only through a multiple-input model that includes all the parameters. Consequently, model M_1 was expanded to include the North Pacific principal atmospheric pattern as an input parameter:

MODEL M_2

$d_1(t)$ = local atmospheric pressure
$d_2(t)$ = local longshore wind stress
$d_3(t)$ = local onshore wind stress
$d_4(t)$ = basin-wide principal atmospheric pattern.

The results are summarized in Table 4. The hindcast skills are shown by the open circles in Fig. 17. The increased estimation skill was generally found to be small (less than 10% at all stations and less than 5% at 12 out of the 20 stations). However, adding the principal atmospheric pattern to the statistical model contributes some very important dynam-

TABLE 4. Hindcast skills, 95% significance levels (in parentheses) and response coefficients for model M_2 (see text). Error bars as in Table 3. Units of the principal atmospheric pattern (input 4) correspond to centimeters of SLH rise when the atmospheric pressure associated with the pattern is −1 mb at the center of the pattern.

Station	S_H	β_1 (cm mb^{-1})	β_2 (cm^3 dyn^{-1})	β_3 (cm^3 dyn^{-1})	β_4 (cm mb^{-1})
Attu	0.07 (0.063)	0.25 ± 0.28	0.20 ± 2.38	0.17 ± 1.76	0.27 ± 0.32
Adak	0.10 (0.058)	0.21 ± 0.23	0.92 ± 2.02	−0.45 ± 2.09	0.34 ± 0.33
Unalaska	0.24 (0.053)	0.08 ± 0.22	1.15 ± 2.07	−1.11 ± 2.13	0.48 ± 0.34
Kodiak	0.18 (0.042)	−0.06 ± 0.15	−0.10 ± 1.81	−0.76 ± 1.21	0.32 ± 0.25
Yakutat	0.29 (0.056)	−0.24 ± 0.22	−0.28 ± 2.84	1.87 ± 2.14	0.38 ± 0.28
Sitka	0.30 (0.041)	−0.20 ± 0.19	0.37 ± 1.74	0.83 ± 1.68	0.37 ± 0.20
Prince Rupert	0.31 (0.035)	−0.38 ± 0.26	0.31 ± 2.18	0.31 ± 1.91	0.41 ± 0.23
Tofino	0.42 (0.036)	−0.63 ± 0.29	1.60 ± 3.13	0.37 ± 2.12	0.24 ± 0.24
Neah Bay	0.46 (0.032)	−0.81 ± 0.28	0.77 ± 2.45	0.27 ± 2.81	0.22 ± 0.24
Astoria	0.34 (0.040)	−0.62 ± 0.42	3.15 ± 3.13	4.90 ± 3.57	0.06 ± 0.28
Crescent City	0.40 (0.033)	−0.72 ± 0.42	2.49 ± 1.96	−1.02 ± 3.22	0.16 ± 0.21
San Francisco	0.27 (0.048)	−0.88 ± 0.54	1.54 ± 2.89	−1.35 ± 3.80	0.13 ± 0.19
Avila Beach	0.05 (0.049)	−0.35 ± 0.69	0.90 ± 3.44	−2.42 ± 4.25	0.12 ± 0.18
Los Angeles	0.06 (0.028)	−0.50 ± 0.54	1.04 ± 3.11	−2.03 ± 3.50	0.14 ± 0.12
San Diego	0.08 (0.042)	−0.58 ± 0.68	0.37 ± 3.15	−4.38 ± 5.05	0.11 ± 0.15
Ensenada	0.09 (0.041)	−0.64 ± 0.62	−0.50 ± 2.94	0.27 ± 5.39	0.15 ± 0.14
La Paz	0.11 (0.129)	−1.00 ± 1.55	0.43 ± 8.92	−7.12 ± 15.06	0.20 ± 0.28
Mazatlan	0.20 (0.083)	−1.56 ± 1.91	8.33 ± 10.68	−2.69 ± 15.11	0.37 ± 0.35
Manzanillo	0.16 (0.093)	−1.81 ± 2.23	6.04 ± 14.59	−7.93 ± 15.85	0.39 ± 0.37
Acapulco	0.10 (0.068)	−1.94 ± 1.84	8.18 ± 10.09	11.12 ± 15.12	0.24 ± 0.34

ical information. Table 4 shows that the coupling coefficients of local pressure and local onshore wind stress are quite stable; the values obtained in model M_2 do not differ significantly from those obtained in model M_1. In contrast, the response to local longshore wind stress changes considerably when the effects of basin-wide winds are included in the model (especially at the northern stations). The coupling coefficients of the principal atmospheric pattern and the local longshore wind stress are shown in Fig. 19 for model M_2. The large error bars demonstrate the difficulty in separating the effects of both inputs because of the high correlation between the two. The magnitude of response to local longshore wind stress is generally reduced from the value obtained when the principal atmospheric pattern is excluded from the model (shown by the dashed line), indicating that much of the apparent response of SLH to local wind stress shown in Fig. 18 really reflects the effects of basin-wide winds over these monthly time scales.[1] That is, the short space scale aspects of local longshore wind stress, which are uncorrelated between neighboring stations, are relatively unimportant to the dynamics over monthly time scales. The notable exception is the region around the California/Oregon border where the response to local longshore wind stress remains quite large suggesting the importance of local upwelling as opposed to larger scale wind forcing. Otherwise there is no longer a general pref-

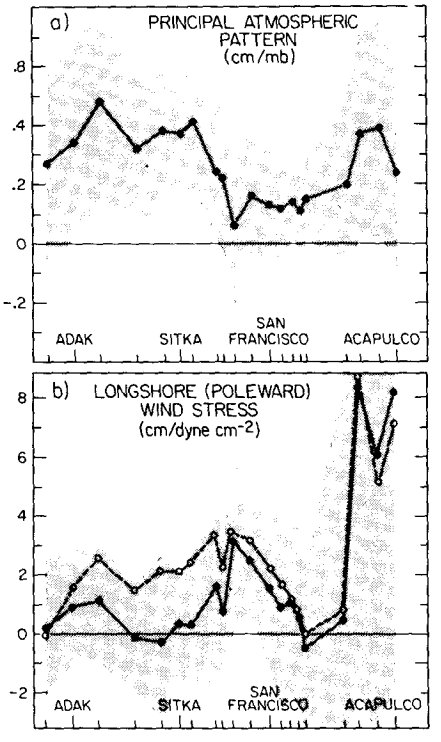

FIG. 19. Spatial distribution of the response coefficients between SLH and (a) the amplitude of the North Pacific principal atmospheric pattern (units correspond to centimeters of SLH rise when the atmospheric pressure associated with the pattern is −1 mb at the center of the pattern); and (b) the longshore component of local wind stress in model M_2. Response coefficients of other inputs are similar to those in Fig. 18. Dashed line in (b) corresponds to the longshore wind stress response coefficient for model M_1 in Fig. 18 and shaded areas correspond to the approximate 90% confidence regions.

[1] An alternative possible interpretation of this statistical result is that the basin-wide atmospheric pattern may be a better representation than the FNOC winds of the actual longshore winds over the shelf.

TABLE 5. Hindcast skills, 95% significance levels (in parentheses) and response coefficients for model M_3 (see text). Error bars as in Table 3.

Station	S_H	β_1 (cm mb^{-1})	β_2 (cm^3 dyn^{-1})	β_3 (cm^3 dyn^{-1})	β_4 (cm mb^{-1})	β_5 (cm cm^{-1})
Attu	0.13 (0.227)	0.33 ± 0.54	0.23 ± 4.57	0.50 ± 3.36	0.41 ± 0.63	−0.19 ± 0.47
Adak	0.47 (0.072)	0.08 ± 0.26	0.83 ± 2.29	0.29 ± 2.38	−0.03 ± 0.40	0.68 ± 0.29
Unalaska	0.36 (0.070)	0.06 ± 0.26	1.62 ± 2.41	−0.90 ± 2.46	0.27 ± 0.42	0.66 ± 0.40
Kodiak	0.34 (0.103)	0.07 ± 0.24	0.29 ± 2.87	−0.65 ± 1.90	0.18 ± 0.41	0.40 ± 0.27
Yakutat	0.71 (0.055)	−0.03 ± 0.23	0.40 ± 2.86	1.29 ± 2.16	0.02 ± 0.31	0.89 ± 0.30
Sitka	0.63 (0.058)	0.00 ± 0.24	0.95 ± 2.11	1.08 ± 2.02	0.12 ± 0.26	0.55 ± 0.21
Prince Rupert	0.55 (0.037)	−0.06 ± 0.29	1.24 ± 2.29	2.02 ± 2.08	0.16 ± 0.25	0.62 ± 0.23
Tofino	0.60 (0.040)	−0.24 ± 0.35	2.47 ± 3.36	−0.72 ± 2.31	0.20 ± 0.26	0.44 ± 0.19
Neah Bay	0.60 (0.039)	−0.44 ± 0.36	0.86 ± 2.71	−1.06 ± 3.17	0.18 ± 0.27	0.43 ± 0.20
Astoria	0.58 (0.047)	−0.23 ± 0.51	2.23 ± 3.46	6.58 ± 4.00	0.05 ± 0.31	0.47 ± 0.30
Crescent City	0.59 (0.041)	−0.28 ± 0.51	2.18 ± 2.19	1.00 ± 3.69	0.09 ± 0.23	0.62 ± 0.26
San Francisco	0.43 (0.085)	−0.55 ± 0.72	1.15 ± 3.87	0.78 ± 5.15	0.04 ± 0.26	0.44 ± 0.27
Avila Beach	0.53 (0.044)	0.11 ± 0.67	1.29 ± 3.29	−0.74 ± 4.08	0.01 ± 0.17	0.79 ± 0.23
Los Angeles	0.78 (0.039)	−0.05 ± 0.64	−1.52 ± 3.70	0.71 ± 4.16	0.05 ± 0.14	0.85 ± 0.18
San Diego	0.67 (0.015)	−0.15 ± 0.41	1.70 ± 1.88	−2.92 ± 3.02	0.01 ± 0.09	0.90 ± 0.12
Ensenada	0.47 (0.032)	−0.48 ± 0.56	0.56 ± 2.65	−0.23 ± 4.84	0.06 ± 0.13	0.52 ± 0.15
La Paz	0.52 (0.103)	−0.21 ± 1.46	−2.27 ± 8.22	−1.16 ± 13.84	0.01 ± 0.27	0.46 ± 0.21
Mazatlan	0.76 (0.089)	0.18 ± 2.14	3.91 ± 11.29	3.15 ± 16.01	0.11 ± 0.38	0.85 ± 0.31
Manzanillo	0.69 (0.083)	−0.12 ± 2.22	13.42 ± 14.10	−6.59 ± 15.22	0.21 ± 0.37	0.73 ± 0.27

erence of local longshore wind stress over the onshore component. Note that Wang and Mooers (1977) also found local atmospheric forcing to be important in this region (from San Francisco to a point about 200 km north of Crescent City) at shorter periods of around 10 days. They attribute the response to a resonant interaction between wind and poleward propagating coastal trapped waves.

The response of SLH to local atmospheric pressure is still significantly greater than inverse barometric from Yakutat to San Francisco after including the effects of basin-wide winds. The possibility remains that the additional response to pressure may reflect a correlation of pressure with another variable omitted from the statistical model. The only remaining obvious local atmospheric parameter is the wind-stress curl. As discussed earlier, scaling arguments suggest that the effect of wind-stress curl on coastal SLH variability should be small. Indeed, it was found that addition of the local wind-stress curl to model M_2 did not significantly increase the estimation skill (<2% increase at all stations) nor alter the response coefficient of the local atmospheric pressure.[2] In fact, with the exceptions of Tofino, Neah Bay and San Francisco where it decreased only slightly, the non-barometric response of SLH increased a small amount at all stations (and the error bars increased 50–75%, reflecting the strong correlation between atmospheric pressure and wind-stress curl).

These results can be taken as an indication that the apparent non-barometric response of SLH cannot be attributed to correlations of atmospheric pressure with any *local* atmospheric forcing parameter. Motivated by the earlier simple dynamical discussion [Eq. (4)], model M_2 was extended to include SLH at the adjacent station to the south as an input:

MODEL M_3

$d_1(t)$ = local atmospheric pressure
$d_2(t)$ = local longshore wind stress
$d_3(t)$ = local onshore wind stress
$d_4(t)$ = basin-wide principal atmospheric pattern
$d_5(t)$ = SLH at adjacent station to the south

Note that, to avoid redundancy of inputs by including both the local longshore wind stress and the average longshore wind stress between the estimand station and the adjacent station to the south [as suggested from Eq. (4)], the latter has been omitted from model M_3. Substitution of average wind stress for local wind stress did not alter the results. Also, because of the close proximity of Tofino and Neah Bay, Astoria SLH was used as the input for statistical estimation of SLH at Tofino. The results of model M_3 are summarized in Table 5 and shown in Figs. 20 and 22.

Except at Attu, the increases in hindcast skill in model M_3 are dramatic (see Fig. 20), ranging from a 20–40% increase at stations north of San Francisco to a 50–70% increase at stations to the south. Before examining the response coefficients in model M_3 in detail, it is useful to determine whether these increased estimation skills reflect the effects of locally wind forced coastal trapped wave dynamics. As discussed earlier, the importance of wave-like processes in adjusting the system to the steady-state balance

[2] The wind-stress curl data used here were computed by FNOC from the quasi-geostrophic wind stress data described in Section 3. Six-hourly values of quasi-geostrophic wind-stress curl were averaged to form monthly mean values on the standard FNOC grid.

(3) can be determined by formulating the statistical model (5). Longshore differences (slopes) in sea level should be positively correlated with the average wind stress between the two stations.

The correlations between Δh and $\bar{\tau}^y$ for neighboring station pairs from Attu to San Diego are shown in Fig. 21. (None of the correlations farther south were statistically significant.) The results are similar to those obtained by Enfield and Allen (1980) (recall that the wind stress data used in this study differs from that used by Enfield and Allen). With the exception of the SLH difference between Astoria and Crescent City, the correlations between Δh and $\bar{\tau}^y$ are statistically significant from Prince Rupert to Los Angeles. The poor relation between Astoria and Crescent City may indirectly be due to the strong effects of onshore wind stress at Astoria (see models M_1 and M_2) which is correlated with the longshore wind stress. The correlation between Δh from Neah Bay to Crescent City and the average longshore wind stress *is* significant (see open circle in Fig. 21).

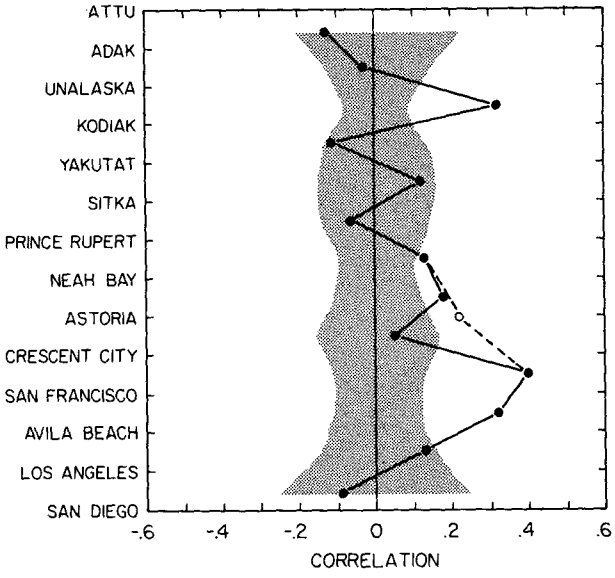

FIG. 21. Correlation between longshore differences of SLH between neighboring stations and the average longshore wind stress between the two stations. Shaded region represents range of correlation values for which statistical significance is less than 95%. These significance levels were estimated from squared correlation (skill) values as described in Section 2. Open circle represents correlation of the sea-level difference between Neah Bay and Crescent City with the average longshore wind stress between the two stations.

Although the correlations from Prince Rupert to Los Angeles are statistically significant, they are quite small, accounting for only 5–15% of the variance of longshore sea-level slope between neighboring stations. Locally wind forced coastal trapped waves therefore appear to be only marginally important to the dynamics along the west coast of North America. This conclusion is perhaps not totally surprising in view of the results of Section 4 where it was shown that the dominant response of SLH to large-scale winds was a universal rise/fall rather than a longshore tilt. Additional evidence that the dynamical balance (5) does not appear to be very important is the fact that the amplitude time series of the fourth EOF of SLH (Fig. 4), which does somewhat resemble a large-scale tilt of SLH, is found to be only weakly correlated with the basin-wide wind pattern in Fig. 6 (a correlation of 0.19 compared with a 95% significance level of 0.10).

These results and dynamical considerations suggest that most of the increased estimation skills in model M_3 are due to the close relation between SLH at neighboring stations from the presence of long, free waves rather than locally wind-forced, poleward propagating coastal trapped waves. If, in fact, wave-like dynamics are responsible for the high estimation skills of model M_3, we might expect SLH at a given location to be more closely related to SLH at the adjacent station to the south than to SLH at the adjacent station to the north, if for no other reason than because of the effects of dissipation on the poleward propagating disturbances. As a test of this hypothesis, model M_3 was modified by replacing the fifth input parameter with SLH at the adjacent station to the north:

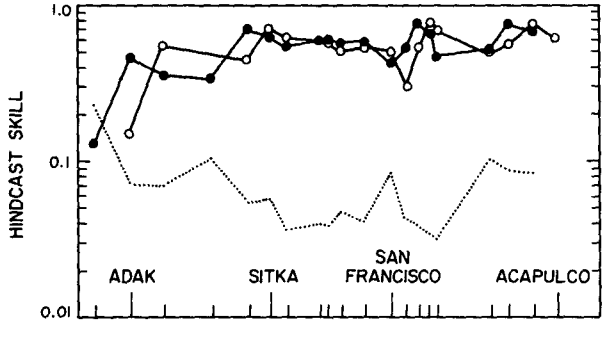

FIG. 20. Skill in estimating SLH from model M_3 (solid circles) and model M_4 (open circles). Dotted line corresponds to the 95% significance level for the hindcast skill values of model M_3.

MODEL M_4

$d_1(t)$, $d_2(t)$, $d_3(t)$, $d_4(t)$ = same as model M_3
$d_5(t)$ = SLH at adjacent station to the north.

The estimation skills are similar to those obtained from model M_3 (see open circles in Fig. 20). (Note the significant decrease in model M_4 estimation skill at Adak, again emphasizing the independence of SLH behavior at Attu.) The fact that addition of either SLH at the adjacent station to the south or north improves the hindcast skill over model M_2 is an indication that much of the residual SLH not accounted for by purely local forcing is very large scale (long wavelength). However, since there is no

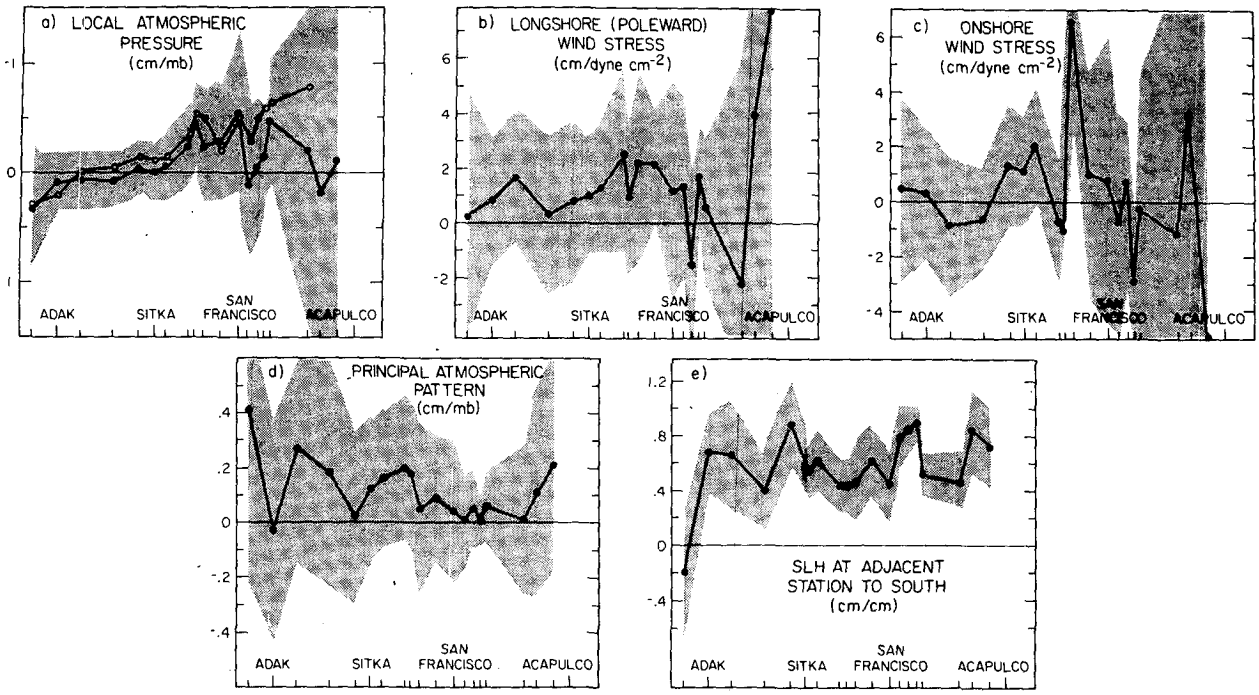

FIG. 22. Spatial distribution of the response coefficients for the inputs of model M_3. Shaded region corresponds to the 90% confidence limits. Units of principal atmospheric pattern response coefficient are the same as in Fig. 19. Open circles in (a) represent response coefficients of local atmospheric pressure in model M_5.

obvious general preference of model M_3 over model M_4, we cannot conclude that the increased skill is due entirely to poleward propagating wave-like phenomena. Equally plausible explanations from the results of these statistical models are equatorward propagating wave-like disturbances or a simultaneous large-scale rise or fall of SLH (no propagation). The only piece of evidence supporting poleward propagation as the preferred mechanism is the statistical result of Section 4 suggesting poleward propagation of very low frequency El Niño related phenomena with phase speeds of about 40 cm s^{-1} (Fig. 12).

Returning to model M_3, the response coefficients of SLH at the adjacent station to the south are shown in Fig. 22e. Note the poor relationship between Attu and Adak. Elsewhere, values generally range from about 0.5 to 0.8. The fact that the values are all less than 1 might be expected for poleward propagating disturbances when the effects of dissipation are taken into consideration. The same reasoning would anticipate that the response coefficient of SLH at the adjacent station to the north in model M_4 would be greater than 1. However, this turns out not to be the case; the values are less than 1 at all locations, similar to those obtained in model M_3. Again, from these results it is not possible to detect any preference for poleward as opposed to equatorward propagation in the coupling between SLH at neighboring stations.

The responses of SLH to longshore and onshore wind stress (Figs. 22b and 22c) are not significantly altered from model M_2 by the addition of SLH at the adjacent station to the south. In contrast, the responses to the principal atmospheric pattern (Fig. 22d) are reduced to about 50–75% of the responses in model M_2. A probable explanation for this change in the apparent response to these basin-wide winds is that the low-frequency (interannual) aspects of this large-scale atmospheric variability are found to be significantly correlated (0.4) with the eastern tropical Pacific El Niño index shown in Fig. 11. It was demonstrated in Section 4 that part of the SLH variability at each station is related to poleward propagation of this El Niño phenomenon. These effects are accounted for in the statistical model when SLH at a neighboring station is included (as in models M_3 and M_4). However, when neighboring SLH is omitted from the model (as in model M_2) part of the apparent response to the principal atmospheric pattern will actually reflect a response to El Niño related effects not directly accounted for in the model. This again emphasizes the importance of including all of the forcing parameters in a multiple input statistical model.

The most important change introduced by the addition of SLH at the adjacent station to the south to the statistical model is the reduction of the response to local atmospheric pressure (Fig. 22a). The error bars on the estimated response coefficients are still large due to the fundamentally limited accuracy

with which responses can be estimated from finite record lengths when the number of correlated forcing parameters becomes large. However, although the responses are still slightly larger than inverse barometric from Tofino to San Francisco, with the exception of Neah Bay, they are no longer statistically different from zero within the 90% confidence limits. This would seem to indicate that part of the apparent non-barometric response of SLH in models M_1 and M_2 resulted from a correlation of local pressure with SLH at the adjacent station to the south or, probably more precisely, a correlation with some atmospheric parameter which forces SLH to the south.

Past theoretical studies of forced coastal trapped waves suggest two possible candidates for the responsible atmospheric parameter. Atmospheric pressure fluctuations were the generating mechanism originally proposed by Robinson (1964). However, more recent studies by Adams and Buchwald (1969) and Gill and Schumann (1974) have shown through scaling arguments that longshore wind stress should be more efficient than local pressure in forcing coastal trapped waves. They argue that the apparent generation of coastal trapped waves by pressure demonstrated in earlier studies (e.g., Hamon, 1966) really reflects generation by the longshore wind stress which is correlated with pressure. Wang and Mooers (1977) attempted to determine from observations which atmospheric parameter was responsible for coastal trapped wave generation along the west coast of the United States. They found poleward propagating SLH disturbances to be more closely related to resonant forcing by atmospheric pressure than to measured wind speed. They suggested that the winds used in their analysis were strongly influenced by orographic effects and were therefore not representative of large-scale wind forcing over the continental shelf, in which case the important aspects of the wind might be better represented in the pressure data than in wind measured at the coast. It therefore appears that the wind-forcing mechanism has not yet been demonstrated to be more appropriate than the originally proposed atmospheric pressure-forcing mechanism.

The phase speeds of the coastal trapped waves likely to be generated by atmospheric forcing (100–400 km day^{-1}) are too large for propagation to be detected in the monthly SLH averages examined here. Resonant forcing of these waves is more appropriately studied from daily sampled data. However, we can attempt to determine whether wind forcing at locations to the south is in fact responsible for the model M_3 reduction of apparent SLH response to atmospheric pressure by replacing SLH at the adjacent station to the south with longshore wind stress to the south. In order to limit the number of inputs, only the longshore wind stress at the three adjacent stations to the south will be included in the model:

MODEL M_5

$d_1(t)$, $d_2(t)$, $d_3(t)$, $d_4(t)$ = same as model M_3
$d_5(t)$ = longshore wind stress at adjacent station to the south
$d_6(t)$ = longshore wind stress two stations to the south
$d_7(t)$ = longshore wind stress three stations to the south.

The resulting estimation skills and response coefficients are summarized in Table 6. Note that the hindcast skills for model M_5 are considerably lower than for model M_3 and only slightly higher than for model M_2 (with a substantial decrease in statistical significance). Note also the large error bars on the response coefficients of the wind-stress parameters; because of the high degree of correlation between longshore wind stress at neighboring stations, the response of SLH to each individual wind-stress parameter cannot be estimated with any useful accuracy. The error bars on the response coefficients of local atmospheric pressure also increase somewhat over those of model M_3 which frustrates attempts to determine whether the response to pressure is significantly reduced in model M_5. However, the values of the pressure response coefficients are all smaller than those obtained in model M_2 and are generally only slightly larger than those obtained in model M_3 (see Fig. 22a). Thus, it appears that at least part of the apparent non-barometric SLH response in models M_1 and M_2 may indeed be related to wind forcing at neighboring stations to the south.

Efforts to determine whether atmospheric pressure forcing at adjacent stations to the south could also account for part of the apparent non-barometric response in models M_1 and M_2 were unsuccessful. Because of the high correlations between atmospheric pressure at neighboring stations, the error bars on the local pressure response coefficients became excessively large when neighboring pressures were included as inputs in the statistical model.

7. Conclusions

The similarity between dynamical and statistical models discussed in Section 2 provides a means for investigating existing theoretical models of coastal dynamics. If the true dynamics are deterministic, the statistical model recovers the dynamical transfer functions between the inputs and the output. Since these theoretical models can be expressed in terms of the sea surface elevation, monthly means of sea level can be used to examine coastal dynamics over short-term climatic time scales of months to years.

The results of Section 3 indicate that the dominant scales of SLH are extremely large spatially and predominantly low frequency. Approximately 40% of

TABLE 6. Hindcast skills, 95% significance levels (in parentheses) and response coefficients for model M_5 (see text). Error bars as in Table 3.

Station	S_H	β_1 (cm mb^{-1})	β_2 (cm^3 dyn^{-1})	β_3 (cm^3 dyn^{-1})	β_4 (cm mb^{-1})	β_5 (cm^3 dyn^{-1})	β_6 (cm^3 dyn^{-1})	β_7 (cm^3 dyn^{-1})
Attu	0.08 (0.115)	0.29 ± 0.51	0.18 ± 4.84	0.49 ± 3.32	0.35 ± 0.69	−0.10 ± 8.57	0.69 ± 7.84	−1.41 ± 4.99
Adak	0.16 (0.100)	0.20 ± 0.44	−1.12 ± 7.54	−0.11 ± 4.35	0.54 ± 0.65	2.71 ± 9.36	−0.87 ± 5.90	−3.30 ± 5.75
Unalaska	0.25 (0.118)	−0.02 ± 0.51	1.07 ± 3.23	−1.42 ± 3.76	0.45 ± 0.69	1.78 ± 6.27	−2.94 ± 8.95	0.64 ± 7.15
Kodiak	0.20 (0.070)	−0.05 ± 0.26	−0.96 ± 3.13	−0.50 ± 2.01	0.28 ± 0.34	1.60 ± 4.94	−3.00 ± 4.78	2.76 ± 4.29
Yakutat	0.35 (0.093)	−0.14 ± 0.35	−2.90 ± 6.90	1.52 ± 4.28	0.25 ± 0.43	3.11 ± 9.40	−1.12 ± 8.33	3.31 ± 5.35
Sitka	0.39 (0.058)	−0.11 ± 0.33	0.52 ± 4.28	1.76 ± 2.80	0.21 ± 0.28	−0.94 ± 5.43	3.54 ± 4.90	1.33 ± 4.48
Prince Rupert	0.43 (0.052)	−0.14 ± 0.44	−1.51 ± 3.21	1.59 ± 2.65	0.21 ± 0.31	4.10 ± 5.66	3.23 ± 6.08	−0.01 ± 3.29
Tofino	0.46 (0.050)	−0.36 ± 0.46	−1.56 ± 5.15	−0.17 ± 3.98	0.20 ± 0.30	4.22 ± 7.68	−0.42 ± 5.47	2.39 ± 5.45
Neah Bay	0.49 (0.048)	−0.53 ± 0.46	−1.28 ± 5.10	1.64 ± 4.20	0.18 ± 0.30	1.81 ± 7.79	1.00 ± 5.56	0.71 ± 5.53
Astoria	0.35 (0.056)	−0.50 ± 0.63	1.42 ± 5.54	5.40 ± 5.10	0.03 ± 0.34	1.35 ± 6.76	2.38 ± 9.38	−2.74 ± 8.24
Crescent City	0.45 (0.052)	−0.21 ± 0.72	2.19 ± 4.47	0.81 ± 4.92	0.20 ± 0.27	−2.27 ± 8.35	9.70 ± 10.72	−5.96 ± 8.97
San Francisco	0.30 (0.075)	−0.51 ± 0.90	−1.56 ± 5.94	−0.97 ± 5.85	0.17 ± 0.25	6.86 ± 10.38	−3.99 ± 13.22	1.03 ± 8.00
Avila Beach	0.07 (0.092)	−0.29 ± 0.99	−1.29 ± 8.67	−0.60 ± 7.94	0.13 ± 0.26	1.46 ± 14.91	1.48 ± 8.87	3.71 ± 7.99
Los Angeles	0.10 (0.048)	−0.50 ± 0.72	−2.50 ± 6.77	−1.19 ± 4.87	0.13 ± 0.15	2.92 ± 5.73	−1.60 ± 6.37	4.43 ± 4.84
San Diego	0.11 (0.061)	−0.59 ± 0.84	−0.10 ± 6.59	−2.52 ± 7.16	0.10 ± 0.18	0.52 ± 6.68	−1.36 ± 7.44	4.16 ± 5.64
Ensenada	0.16 (0.056)	−0.64 ± 0.75	0.41 ± 3.65	3.32 ± 7.12	0.13 ± 0.16	−4.91 ± 7.20	6.56 ± 5.02	0.86 ± 6.85
La Paz	0.20 (0.154)	−0.79 ± 1.75	−6.55 ± 14.44	−7.49 ± 16.94	0.21 ± 0.32	7.87 ± 10.14	3.50 ± 17.33	0.57 ± 6.10

the variability consists of a general rise or fall of sea level with remarkably constant amplitude everywhere from the Aleutian Islands to Mexico. The atmospheric variability is also very large spatially but, in contrast to SLH, consists of a more nearly uniform distribution of time scales.

The nature of this large scale SLH variability (as represented by the principle empirical orthogonal function) was examined in Section 4. It was concluded that the response can be broken down into two primary frequency bands: the ocean at middle and tropical latitudes is highly coupled at the lower frequencies; and the SLH variability at frequencies < 1 cpy is very closely related to El Niño phenomena in the eastern tropical Pacific. Evidence was presented for northward propagation of these El Niño related effects at phase speeds of $\sim$40 cm s^{-1}. The SLH response at frequencies > 1 cpy can be attributed to the direct effects of atmospheric forcing. The response is similar to that expected for large-scale wind-driven quasi-geostrophic currents. Cyclonic basin-wide winds cause a rise in SLH along the entire west coast of North America that tends to persist for a time period of several months.

The very low frequency secular variability of SLH was examined in Section 5. SLH has generally been rising at the southerly stations and dropping along the coast of southeastern Alaska. It was suggested that at least part of this drop in measured SLH may be due to a cooling of the surface waters in the northern North Pacific rather than totally from isostatic rebound of the earth's crust as is generally assumed.

Much of the non-secular raw SLH variability at stations north of San Francisco is due to the simple inverse barometric response to local atmospheric pressure (50–60% of the total variance). These inverted barometer effects account for only 10–15% of the variance at stations to the south. The local aspects of dynamic (inverse-barometer-corrected) SLH variability were examined in Section 6 through a hierarchy of statistical models and the results were compared with simple existing dynamical models. It was shown that local atmospheric forcing accounts for 20–40% of the pressure-corrected SLH variance at stations north of San Francisco and less than 10% at stations to the south. Except at stations in large, semi-enclosed basins, the longshore wind stress forces a larger SLH response than onshore wind stress, and the response is consistent with that expected from Ekman dynamics. Over these monthly time scales, basin-wide aspects of the wind field appear to generally be more important than local aspects. A steady-state balance of forces between the longshore wind stress and a longshore SLH tilt was shown to be only moderately valid from Prince Rupert to Los Angeles. The response to longshore winds appears to be more nearly a large-scale rise/fall than a tilt of SLH.

Addition of neighboring SLH to the local atmospherically forced model increases the estimation skills; 50–80% of the SLH variance can be accounted for from Adak to Acapulco. These large increases in estimation skill indicate that the residual SLH not related to local atmospheric forcing has very large spatial scale. Attempts to determine whether this was due to long-wavelength, poleward-propagating free coastal trapped waves were inconclusive; SLH at a given station can be estimated equally well from SLH to the north or south.

Part of an apparent non-barometric response of SLH to local pressure in purely locally driven statistical models was shown to actually represent an influence of SLH farther south. This emphasizes the risk of deducing misleading cause-and-effect relationships when not all of the important forcing parameters have been included in the model. The relation between local atmospheric pressure at a given station and SLH at the adjacent station to the south presumably reflects effects of atmospheric forcing at the southern stations. Efforts to determine the responsible aspect of southern atmospheric forcing were somewhat limited by the fact that all potential driving forces are highly correlated. This results in an inability to estimate accurately the response to each individual forcing parameter. However, evidence was presented suggesting that some of the apparent non-barometric response in purely locally driven models was due to forcing by the longshore wind stress at stations to the south.

Possibly one of the most important conclusions from this study is that it is extremely difficult to accurately estimate the individual responses of any dynamical variable to a number of correlated forcing functions. The error bars on the statistically estimated response coefficients increase rapidly as the number of inputs included in the model increases and as the various inputs become more highly intercorrelated. In effect, the usefulness of the statistical model for examining dynamical relationships diminishes as the statistical model becomes more complex. This presents somewhat of a dilemma: On the one hand, it is desirable to minimize the number of inputs in the statistical model in order to maximize statistical significance; on the other hand, all the appropriate inputs must be included in the statistical model in order not to draw erroneous conclusions about cause and effect. The only method for increasing the statistical reliability of estimated response coefficients in a given model is to increase the record length.

Acknowledgments. We wish to thank Klaus Wyrtki for compiling and archiving the sea-level data and the Fleet Numerical Oceanography Center for generating the atmospheric data used in this study. The help of Steve Pazan in securing these data is gratefully acknowledged. Helpful comments from Dave Enfield, John Allen and Allan Clarke are also appreciated.

We wish to thank Sandi Thomas for her patience in typing initial and subsequent drafts of this manuscript.

This research was partially sponsored by the Office of Naval Research under Contract N00014-79-C0152 as part of the NORPAX program at Scripps Institution of Oceanography and partially by the Jet Propulsion Laboratory, California Institute of Technology, under NASA Contract NAS7-100.

APPENDIX

Objective Technique for Low-Pass Filtering in the Presence of Data Gaps

A commonly implemented low-pass filter is the $(2M + 1)$ month running mean which, for a monthly sampled time series $h(t)$, is given by

$$h_1(t) = \frac{1}{2M+1} \sum_{t-M}^{t+M} h(t') \qquad \text{(A1)}$$

(see Bracewell, 1978). The frequency response function of the running mean filter [Eq. (A1)] is given as a function of frequency f by

$$H_1(f) = \frac{\text{sinc}[(2M+1)f]}{\text{sinc}f},$$

which is shown by the dotted line in Fig. 23. It can be seen that $h_1(t)$ is a low-pass filtered version of $h(t)$ with periodicities shorter than $(2M + 1)$ months effectively removed. Undesirable features of the running mean filter (A1) are the large side lobes of the frequency response function which can be eliminated by smoothing $h(t)$ for a second time with another $(2M + 1)$ month running mean filter,

$$h_2(t) = \frac{1}{2M+1} \sum_{t-M}^{t+M} h_1(t'). \qquad \text{(A2)}$$

The resulting frequency response function is

$$H_2(f) = \frac{\text{sinc}^2[(2M+1)f]}{\text{sinc}^2 f},$$

shown by the solid line in Fig. 23. The double running mean filter is equivalent to a triangular filter (see Bracewell, 1978) and has a half-power point of about 0.5 cpy.

For a time series $h(t)$ with no missing data, computation of the low-pass filtered time series $h_2(t)$ at time t is straightforward. However, when one or more of the $h(t')$ in the $(2M + 1)$ month average are missing, the running mean in (A1) cannot be computed. The technique used here consists of first forming an objective estimate $h_1^*(t)$ of $h_1(t)$ based on the existing

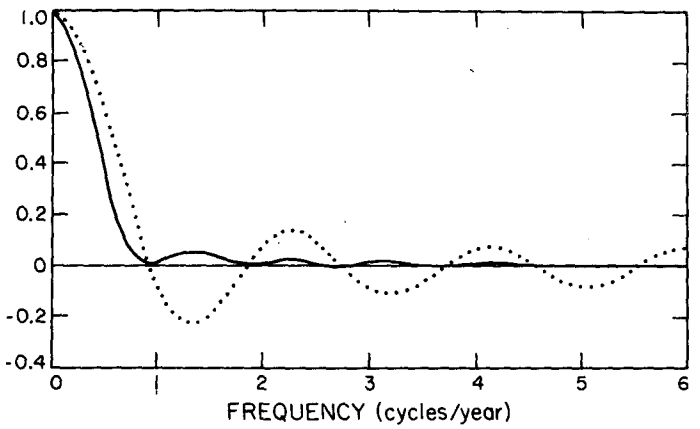

FIG. 23. Transfer function for the 13-month running mean filter (dotted line) and the double 13-month running mean filter (solid line) as a function of frequency.

data values in the $(2M + 1)$ month average by

$$h_1^*(t) = \beta_1(t) \sum_{t-M}^{t+M} h(t^*), \qquad \text{(A3)}$$

where the summation over t^* includes only those times t' in (A1) when $h(t')$ exists. For ease of notation, the limits of all summations hereafter will be assumed to be from $(t - M)$ to $(t + M)$ unless explicitly stated otherwise.

The expected square error of the estimated running mean is given by

$$\{[h_1(t) - h_1^*(t)]^2\} = \{h_1^2(t)\} + \beta_1^2(t) \sum_{t^*} \sum_{s^*} \{h(t^*)h(s^*)\} - \frac{2\beta_1(t)}{2M+1} \sum_{t^*} \sum_{t'} \{h(t^*)h(t')\}, \qquad \text{(A4)}$$

where the braces are used to denote the sample mean value. Again, the summations over quantities with an asterisk include only those times t' in (A1) when $h(t')$ exists. The coefficient $\beta_1(t)$ is determined by minimizing the expected square error of the estimate which leads to

$$\beta_1(t) = \frac{1}{2M+1} \frac{\sum_{t^*} \sum_{t'} \{h(t^*)h(t')\}}{\sum_{t^*} \sum_{s^*} \{h(t^*)h(s^*)\}}. \qquad \text{(A5)}$$

The time-lagged mean products in (A4) and (A5) can be estimated from the sample data by assuming the time series to be stationary so that, for example,

$$\{h(j)h(k)\} = \frac{1}{T} \sum_{t=1}^{T} h(t)h(t + k - j). \qquad \text{(A6)}$$

The summation is over the T times t when both $h(t)$ and $h(t + k - j)$ exist. Using (A5), the expected square error of the objective estimate reduces to

$$\{[h_1(t) - h_1^*(t)]^2\} = \frac{1}{(2M+1)^2} \times \left[\sum_{t'} \sum_{s'} \{h(t')h(s')\} - \frac{[\sum_{t^*} \sum_{t'} \{h(t^*)h(t')\}]^2}{\sum_{t^*} \sum_{s^*} \{h(t^*)h(s^*)\}} \right]. \qquad \text{(A7)}$$

The sample mean products in (A7) can all be evaluated by expressions of the form (A6).

When there are no missing data, (A7) reduces to zero. Note that when there are gaps in the data, the expected square error of the estimate decreases as the square of the running mean filter length. For a given filter length, the accuracy of the objective estimate depends on the number of missing data values in the $(2M + 1)$ month running mean and on the nature of the time series $h(t)$. This can most easily be seen by expressing the expected square error as a fraction of the mean square of the filtered time series h_1, i.e.,

$$\frac{\{[h_1(t) - h_1^*(t)]^2\}}{\{h_1^2(t)\}} = 1 - \frac{[\sum_{t^*} \sum_{t'} \{h(t^*)h(t')\}]^2}{\sum_{t'} \sum_{s'} \{h(t')h(s')\} \sum_{t^*} \sum_{s^*} \{h(t^*)h(s^*)\}}. \qquad \text{(A8)}$$

With an increasing number of missing data values, the number of terms in the numerator of the second term of (A8) decreases and the fractional expected square error approaches 1. This especially becomes

a problem when the time scales of $h(t)$ are short in which case the mean products in (A6) are small except at small lag $(j - k)$. When the time scales of $h(t)$ are large, the mean products in (A6) are large even for large $(j - k)$. Then the effects of missing data becomes less severe (although they become important when the number of missing data becomes large) and the fractional expected square error decreases.

In Section 4, the interest was in interannual aspects of SLH variability which can be extracted by filtering the data with a 13-month running mean, i.e., $M = 6$ in (A1)-(A8). Since SLH variability is dominated by low frequencies (see Fig. 5), even when 6 out of 13 values of $h(t')$ in (A3) were missing, the fractional expected square error never exceeded 10%. With increasing numbers of missing data, the expected error of the estimate increased. Estimates with fractional expected square error exceeding 25% were omitted from the analysis described in Section 4.

Once the 13-month running mean SLH time series $h_1^*(t)$ at each station were estimated by (A3), the data were filtered a second time with another 13-month running mean estimate of the form

$$h_2^*(t) = \beta_2(t) \sum_{t-M}^{t+M} h_1^*(t^*), \qquad \text{(A9)}$$

with $M = 6$. This removes the effects of the side lobes in the frequency response function as discussed earlier. β_2 can be evaluated by an expression exactly analogous to (A5). Again, estimates with fractional expected square error exceeding 25% were omitted from the analysis in Section 4.

Even after removing linear trends in the data (see Section 5) some of the resulting low-pass filtered SLH time series exhibited very low frequency variability (time scales of 8 years or longer) which can probably safely be assumed to be unrelated to El Niño (the signal of interest in Section 4). Most notable are Attu, Adak and Unalaska (see Fig. 2). As discussed in Section 3, much of this low-frequency variability is believed to be related to tectonic processes. For the purposes of examining the relation between El Niño and SLH along the west coast of North America, a band-pass filtering technique is needed to remove this very low frequency "noise." The technique used consists of applying a double 97-month running mean objective estimate using (A3) and (A9) with $M = 48$, thereby producing a very low pass filtered time series with a frequency cutoff of 0.125 cpy. This time series was then subtracted from the double 13-month running mean time series resulting in a band-pass filtered time series consisting only of periodicities between 1 and 8 years. These band-pass filtered time series have been contoured in Fig. 12 and correlations with the El Niño index are shown in Fig. 11. (Ensenada was omitted from the figures because of unusually large expected square errors. No immediate explanation for these errors could be found.)

REFERENCES

Adams, J. K., and V. T. Buchwald, 1969: The generation of continental shelf waves. *J. Fluid Mech.*, **35**, 815–826.

Allison, L. J., J. Steranka, R. J. Holub, J. Hansen, F. A. Godshall and C. Prabhakera, 1972: Air-sea interaction in the tropical Pacific Ocean. NASA Tech. Note D-6684, 84 pp.

Bakun, A., 1973: Coastal upwelling indices, west coast of North America, 1946–71. Tech. Rep. NMFS SSRF-671, NOAA, Seattle, 103 pp.

Bendat, J. S., and A. G. Piersol, 1971: *Random data: Analysis and Measurement Procedures.* Wiley-Interscience, 407 pp.

Bracewell, R. N., 1978: *The Fourier Transform and Its Applications.* McGraw-Hill, 444 pp.

Bretschneider, D. F., and D. R. McLain, 1976: Anomalies of monthly mean sea level along the west coasts of North and South America. *Mar. Fish. Climate,* NOAA, **3**, 95–102.

Brown, W., W. Munk, F. Snodgrass, H. Mofield and B. Zetler, 1975: MODE bottom experiment. *J. Phys. Oceanogr.*, **5**, 75–85.

Cane, M. A., and E. S. Sarachik, 1977: Forced baroclinic ocean motions: II. The linear equatorial bounded case. *J. Mar. Res.*, **35**, 395–432.

Caton, F. G., M. J. Cuming and B. R. Mendenhall, 1978: A northern hemisphere history marine of wind-based parameters. Meteorology International Inc., Tech. Rep. M-231, 106 pp.

Chelton, D. B., 1980: Low frequency sea level variability along the west coast of North America. Ph.D. dissertation, Scripps Institution of Oceanography, University of California, San Diego, 212 pp.

——, 1982: Effects of sampling errors in statistical estimation. *Deep-Sea Res.* (in press).

Clark, J. A., 1977: An inverse problem in glacial geology: The reconstruction of glacier thinning in Glacier Bay, Alaska between A.D. 1910 and 1960 from relative sea level data. *J. Glaciol.*, **18**, 481–503.

Clarke, A. J., 1977: Observational and numerical evidence for wind-forced coastal trapped long waves. *J. Phys. Oceanogr.*, **7**, 231–247.

Crittenden, M. D., 1967: Viscosity and finite strength of the mantle as determined from water and ice loads. *Geophys. J. Roy. Astron. Soc.*, **14**, 261–279.

Davis, R. E., 1976: Predictability of sea surface temperature and sea level pressure anomalies over the North Pacific Ocean. *J. Phys. Oceanogr.*, **6**, 249–266.

——, 1977: Techniques for statistical analysis and prediction of geophysical fluid systems. *Geophys. Astrophys. Fluid Dyn.*, **8**, 245–277.

——, 1978: Predictability of sea level pressure anomalies over the North Pacific Ocean. *J. Phys. Oceanogr.*, **8**, 233–246.

Enfield, D. B., and J. S. Allen, 1980: On the structure and dynamics of monthly mean sea level anomalies along the Pacific coast of North and South America. *J. Phys. Oceanogr.*, **10**, 557–578.

Fissel, D. B., S. Pond and M. Miyake, 1977: Computation of surface fluxes from climatological and synoptic data. *Mon. Wea. Rev.*, **105**, 26–36.

Gill, A. E., and E. H. Schumann, 1974: The generation of long shelf waves by the wind. *J. Phys. Oceanogr.*, **4**, 83–90.

Godfrey, J. S., 1975: On ocean spindown I: A linear experiment. *J. Phys. Oceanogr.*, **5**, 399–409.

Gutenberg, B., 1941: Changes in sea level, postglacial uplift, and

mobility of the Earth's interior. *Geol. Soc. Amer. Bull.*, **52,** 721–772.

Hamon, B. V., 1966: Continental shelf waves and the effects of atmospheric pressure and wind stress on sea level. *J. Geophys. Res.*, **71,** 2883–2893.

Hicks, S., 1978: An average geopotential sea level series for the United States. *J. Geophys. Res.*, **83,** 1377–1379.

——, and W. Shofnos, 1965: The determination of land emergence from sea level observations in southeast Alaska. *J. Geophys. Res.*, **70,** 3315–3320.

Hurlburt, H. E., J. C. Kindle and J. J. O'Brien, 1976: A numerical simulation of the onset of El Niño. *J. Phys. Oceanogr.*, **6,** 621–631.

McCreary, J. P., 1976: Eastern tropical ocean response to changing wind systems: with application to El Niño. *J. Phys. Oceanogr.*, **6,** 632–645.

——, 1977: Eastern ocean response to changing wind systems. Ph.D. dissertation, Scripps Institution of Oceanography, University of California, San Diego, 156 pp.

Namias, J., 1976: Some statistical and synoptic characteristics associated with El Niño. *J. Phys. Oceanogr.*, **6,** 130–138.

O'Conner, J. F., 1961: Mean circulation patterns based on 12 years of Northern Hemisphere data. *Mon. Wea. Rev.*, **89,** 211–227.

Pattullo, J., W. Munk, R. Revelle and E. Strong, 1955: The seasonal oscillation in sea level. *J. Mar. Res.*, **14,** 88–155.

Robinson, A. R., 1964: Continental shelf waves and the response of sea level to weather systems. *J. Geophys. Res.*, **69,** 367–368.

Roden, G. I., 1960: On the nonseasonal variations in sea level along the west coast of North America. *J. Geophys. Res.*, **65,** 2809–2826.

——, 1966: Low frequency sea level oscillations along the Pacific coast of North America. *J. Geophys. Res.*, **71,** 4755–4775.

Saur, J. F. T., 1962: The variability of monthly mean sea level at six stations in the eastern North Pacific Ocean. *J. Geophys. Res.*, **67,** 2781–2790.

Smith, R. L., 1974: A description of current, wind and sea level variations during coastal upwelling off the Oregon coast, July–August 1972. *J. Geophys. Res.*, **79,** 435–443.

Tsumura, K., 1970: Investigation of mean sea level and its variation along the coast of Japan. *J. Geodetic Soc. Japan,* **16,** 239–275.

Wahr, J., and M. Wyss, 1980: Interpretation of post-seismic deformation with a visco-elastic relaxation model. *J. Geophys. Res.*, **85,** 6471–6477.

Wang, D. P., and C. Mooers, 1977: Long coastal trapped waves off the west coast of the United States, summer 1973. *J. Phys. Oceanogr.*, **7,** 856–864.

White, W., K. Hasunuma and G. Meyers, 1979: Large scale secular trend in steric sea level over the western North Pacific from 1954–1974. *J. Geodetic Soc. Japan,* **25,** 49–55.

Wunsch, C., 1972: Bermuda sea level in relation to tides, weather and baroclinic fluctuations. *Rev. Geophys. Space Phys.*, **10,** 1–49.

Wyrtki, K., 1975: El Niño—the dynamic response of the equatorial Pacific Ocean to atmospheric forcing. *J. Phys. Oceanogr.*, **5,** 572–584.